Understanding Magnetic Field Reversal Mechanisms in Mesoscopic Magnetic Multilayer Ring Structures

by

Bryan Ng

B.S., Cornell University (2006)

Submitted to the Department of Materials Science and Engineering
in partial fulfillment of the requirements for the degree of

Master of Science in Materials Science and Engineering

at the

MASSACHUSETTS INSTITUTE OF TECHNOLOGY

September 2008

Author .....
Department of Materials Science and Engineering
August 15, 2008

Certified by .....
Caroline A. Ross
Professor of Materials Science and Engineering
Thesis Supervisor

Accepted by .....
Samuel M. Allen
Chairman, Department Committee on Graduate Theses

Understanding Magnetic Field Reversal Mechanisms in Mesoscopic Magnetic Multilayer Ring Structures

by

Bryan Ng

Submitted to the Department of Materials Science and Engineering
on August 15, 2008, in partial fulfillment of the
requirements for the degree of
Master of Science in Materials Science and Engineering

Abstract

Patterned pseudo spin-valve rings show great promise for device applications due to their non-volatility and variety of stable magnetic states. However, the magnetic reversal of these elements under an applied field is complex due to the magnetostatic coupling between the two ferromagnetic layers.

Elliptical rings are electrically probed using highly symmetric Wheatstone bridges in conjunction with traditional four-point electrical measurements and micromagnetic simulations. New insight into domain wall nucleation and propagation events are elucidated. The resulting behavior is found to yield large signals at very low fields, making these devices ideal for device applications in data storage and computer logic.

360° domain walls are found to be extremely stable until fields as high as 1000Oe, but are positionally uncontrollable in elliptical rings. Rhombic rings were investigated as a geometry that can nucleate, propagate and pin domain walls more easily. Measurements and simulations confirm that the same reversal mechanisms exist and domain walls are more systematically positioned. The control over 360° domain walls is valuable since reversals can occur without nucleation by decoupling the wall into a reverse domain. As a result, rhombic rings are useful as devices that can perform device functions at extremely low fields.

Thesis Supervisor: Caroline A. Ross
Title: Professor of Materials Science and Engineering

Acknowledgments

My time at MIT has undoubtedly been a life-changing experience. Sure, I learned a lot about research, magnetism and nanopatterning, but what I will remember most are the people who shaped my journey through graduate school. These are the people who I will cherish throughout my life, and to whom this thesis is dedicated to.

First and foremost, I would like to thank Professor Ross for the opportunity to work with her and her group. Her open door was always comforting, and her light and witty attitude always brought a smile to my face. I will always appreciate how incredibly supportive she was, being interested not only in my research accomplishments, but also in developing me as a person.

I want to thank the Ross group for their many insightful discussions, open attitudes and fun times. I appreciate the help of Filip Illievski and Irenee Colin, who both taught me much about the lab, fabrication and research. And, I especially appreciate the companionship of Fernando Castaño who was always there with me in lab during the good times and bad. Without his guidance, support, wisdom and insight, I would have only had half as much fun in lab and this thesis would have been significantly shorter.

I could not have made it without the support of my friends, including those from ultimate, the department, around MIT and 2007. It seems as if 2007 was a special year, as I often found these friends of '07 standing by me, eager to pass the time and enjoy the finer moments in life. As the years go on, I know we will continue to share many more memories. Special mention should be made of BHo's computer for helping to run the many micromagnetic simulations used in this thesis.

Finally, I want to thank my family for their love and support. Even though they have little clue of what I am doing, I know that they believe that what I have accomplished is utterly fantastic. I especially want thank Karen Shu for being such a great friend and companion – I couldn't have made it through MIT without you.

Thank you, all of you.

Contents

List of Figures

Chapter 1

Introduction

In 1988, researchers measured large changes in resistance with an applied field in multi-layers of alternating ferromagnetic and non-ferromagnetic metals, terming the behavior "giant magnetoresistance" (GMR) [1, 2]. As a powerful method of exploiting the spin information of electrons, its discovery led to tremendous developments in the field of magnetoelectronics. Perhaps the most significant and ubiquitous use of GMR is as a small and highly sensitive magnetic field sensor in hard disk read heads. The ability to read increasingly small bit regions on a magnetic thin film has allowed storage densities to develop at an incredible rate [3, 4]. It is fitting that the 2007 Nobel Prize in physics was awarded to Grünberg and Fert who first discovered GMR.

Two decades later, GMR continues to play an integral role in next-generation devices. With an increasing understanding of the fundamental principles, GMR-based device concepts have been put forth that challenge even established technologies such as some composite metal oxide semiconductor (CMOS) systems for reduced power consumption and higher efficiency [5, 6]. These concepts use the patterning of magnetic multi-layers as a means of engineering an element's magnetic behavior.

Following the footsteps of the very first core memories [7], one area of active research in magnetic patterning is in nanoscale ring-shaped multi-layer devices since several stable and reproducible states can be induced [8]. This thesis studies the magnetic reversal mechanisms in multi-layered magnetic rings, and attempts to exploit them for device applications. Elliptical rings are first studied. Then, rhombic

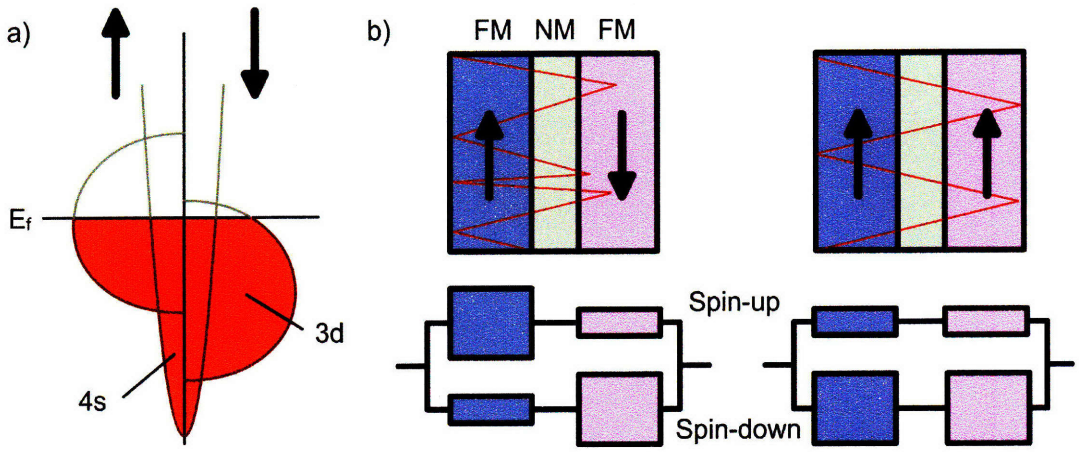

Figure 1-1: a) A representation of the spin-split 3d-band in typical ferromagnetic materials. b) The top half illustrates the ferromagnetic/non-magnetic/ferromagnetic (FM/NM/FM) sequence, including a representation of electron scattering indicated by the red lines. The bottom half shows a simple resistor model for the electrical response.

rings are proposed as a structure to generate and trap 360° domain walls (DWs) instead of commonly observed 180° DWs.

This chapter serves as an introduction to concepts that will be used throughout the thesis, including an explanation of GMR, motivations for patterning GMR multilayers into rings and the use of GMR structures for two specific device applications.

1.1 Giant Magnetoresistance

The majority of metallic ferromagnets, including Ni, Fe and Co, are transition metals that have unoccupied states in their d-bands. Magnetism in these materials arises from the spin-split band structure caused by a quantum mechanical exchange interaction between the electrons (Figure 1-1a). The imbalance in the number of spin-up and spin-down electrons causes a polarization of spin that results in a net magnetization. Electrons moving through these bands do not experience a sizable amount of scattering that flips the spin, but rather experience scattering that varies depending on the type of spin [9]. That is to say, electrons with spin-up have a different scattering probability than spin-down electrons.

In the case of alternating ferromagnetic/non-ferromagnetic layers, GMR is a result

of this spin-dependent scattering and can be thought of as having different resistivity paths for different spins (Figure 1-1b). In one ferromagnetic layer, there will be a low resistance path for one spin of electrons. For convenience, we consider this layer to scatter only spin-down electrons, allowing spin-up electrons to experience low resistance while spin-down electrons have a high resistance. If the magnetization in the second ferromagnetic layer is parallel, then there will also be a low resistance path for spin-up electrons and a high resistance path for spin-down. Current composed of freely moving spin-up electrons will dominate the conduction and create an overall low resistance. On the other hand, if the magnetization in the second ferromagnetic layer is anti-parallel, then there will be a high resistance path for spin-up electrons and a low-resistance path for spin-down electrons. Thus, both types of spin will encounter the same medium resistance and create an overall high resistivity.

In order for GMR to be observed, the thicknesses in the multi-layer require that the mean free path of the electrons is longer than the sum of the layer thicknesses so that the electrons sample the different layers [10]. It should also be noted that the scattering phenomenon is considered to be dominated by an interfacial response rather than a bulk response [11].

1.2 Patterned PSV Elements

Pseudo-spin valves (PSVs) are the simplest GMR multi-layers that comprise of two ferromagnetic layers sandwiching a non-magnetic spacer. One layer is typically made to be magnetically harder than the other so that each switch independently. Hardness can be controlled by using two different materials or by changing layer thicknesses.

A typical PSV is $Ni_{80wt\%}Fe_{20wt\%}$ (NiFe)/Cu/Co, since Co is a magnetically hard material, while NiFe is a magnetically soft material. Typically, only the NiFe would be cycled as a soft/free layer, while the Co is fixed in a certain magnetic state as a hard/reference layer. In an unpatterned polycrystalline film, the magnetization reversal is a balance of exchange energies and magnetostatic energies from the layer interactions. These energies govern the nucleation of domain walls under an applied

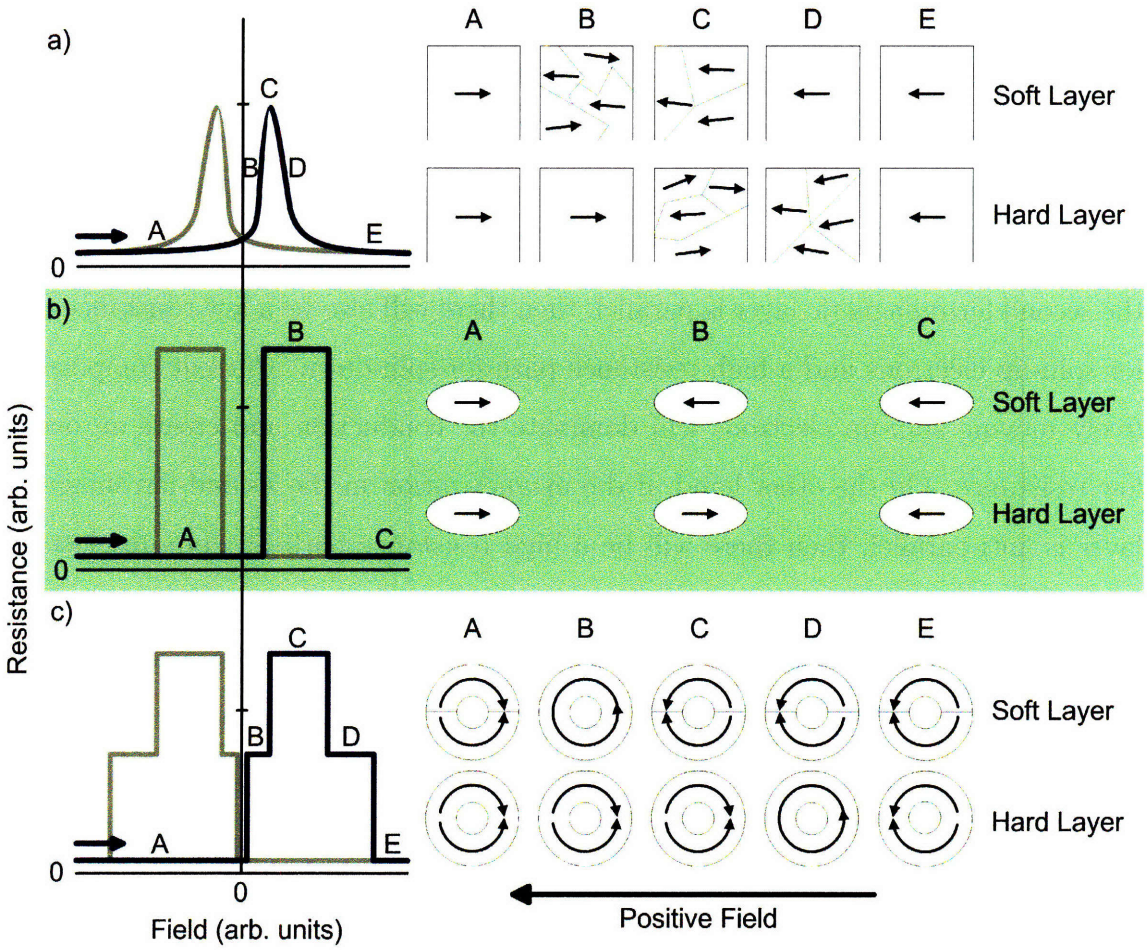

Figure 1-2: Typical overall resistance behavior under applied fields (left), and schematics of the expected magnetic states (right) of a PSV a) film, b) elliptical disk and c) circular ring.

field and reverse in magnetization (Figure 1-2a) [12, 13]. The magnetization reversal in a film is heavily dependent on local film defects that can serve as nucleation and pinning sites for domain walls. Since a bulk film has many nucleation and propagation events, the magnetic trace shows a broad peak at low coercive fields without any sharp transitions. At saturation, both the soft and hard layers can be parallel. However, during reversal, the hard layer begins switching before the soft layer is saturated, and so it is unlikely that the two layers will be completely antiparallel with one another at any given field.

In order to control the magnetization states, shape anisotropy energy can be added by patterning the film. A typical type of pattern is that of an elongated

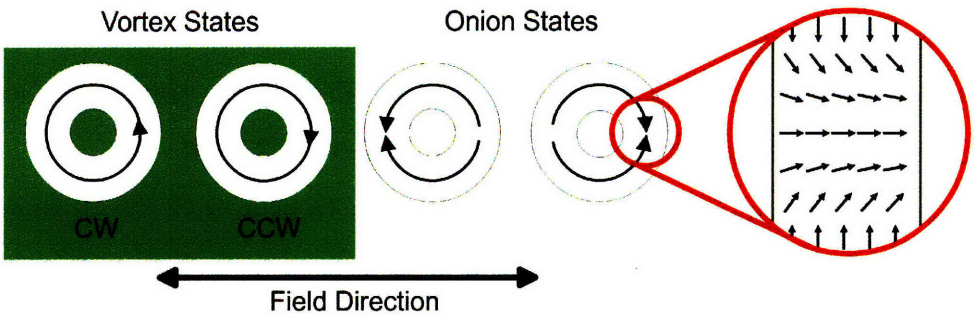

Figure 1-3: Schematic representations of onion and vortex states in a single-layer ferromagnetic ring. Thin metal films and narrow linewidths form transverse Néel walls (inset).

bar or ellipse of submicron dimensions, which tend to switch as a single domain with magnetizations pointed along the long or easy axes (Figure 1-2b) [14]. Since resistance levels are created from the relative alignment of the soft and hard layers, a more distinct GMR response can be produced at more reliable switching fields by confining the magnetization directions to an easy axis.

1.2.1 Circular and Elliptical Rings

Patterning PSVs into circular and elliptical magnetic rings is appealing since there are more stable magnetic states than in bars and discs [15]. To understand the magnetic behavior of the multi-layer behavior, the single-layered ring is first discussed.

Single Layers

Single-layer rings can show two bi-domain onion states, as well as two vortex states of different chiralities with no domain walls (Figure 1-2c). These states have been confirmed experimentally by a myriad of magnetic probing techniques such as magnetic force microscopy [16, 17] and magnetooptical Kerr effect microscopy [18], as well as through electrical probing such as anistotropic magnetoresistance measurements [19] and non-local measurements [20].

Onion states represent the stable structure at saturation and remanence [21]. Two DWs separate two magnetic regions that follow the shape of the ring, but point in the same direction. The type of DW present is highly dependent on the linewidths

of the rings [22]. For thin magnetic rings of under 10nm in thickness and linewidths of less than 200nm, it is expected that DWs are mainly of the transverse Néel type that maintain their magnetizations in-plane (Figure 1-3) [23, 24].

Vortex states are more stable in magnetic rings than in disks since rings avoid the formation of vortex cores which have high exchange energies [25, 26]. The magnetization in these vortex states traverses the circumference without the presence of DWs, and thus produces a flux closed state with no stray fields produced. This is an interesting feature for producing high-density arrays of these elements, since elements can be programmed in a way such that no stray fields are present to interact with an adjacent element.

Vortex states are not necessarily present in ferromagnetic rings, but is rather dependent upon the thicknesses of the layers and the lateral dimensions of the rings [22]. Qualitatively, the stray field energy favors a vortex state while the exchange interaction favors an onion state. Since the stray field energy is dependent on the square of the thickness while the exchange energy increases linearly with the thickness, vortex states tend to be more stable in thick and narrow films while onion states tend to be more stable in thin and wide films [27].

PSV

In order to generate more sizeable electrical signals, multi-layered ring elements are considered in order to use the GMR effect. However, the introduction of an additional layer allows the magnetostatic coupling between the layers to influence switching events and the stable magnetic states associated with them. Unfortunately, it is difficult to magnetically probe both the individual soft and hard layers in a PSV ring concurrently. Thus, results are typically only available for the collective multi-layer with individual layer contributions either modeled or assumed.

As a first approximation, the multi-layer rings can be explained as a superposition of two single-layer rings (Figure 1-2c). Provided that the ring geometry and film thicknesses allow, intermediate states between the two saturated onion states can exist.

Many electrical studies have been performed on NiFe/Cu/Co multi-layers [28, 29, 30, 31] that follow the basic shape of Figure 1-2c). At high fields [A], a saturated state yields two onion states in both layers. On reversing the field, the soft layer may transition into an intermediate state [B] before achieving a high resistance state when the NiFe is in a reverse onion state and both layers are completely antiparallel [C]. With higher fields, the Co switches into an intermediate state [D]. If the resistance is half of the difference between the maximum and minimum values, then the Co is assumed to be in a vortex state, since half of the ring has parallel magnetizations and half the ring has antiparallel magnetizations. At even higher fields, the Co reverses completely and both the soft and hard layers are in reverse onion states [E].

Layered ring elements can therefore exhibit several stable remanent states by toggling the soft layer when the Co layer is in either an onion state, or a vortex state. Clockwise and counter clockwise vortices have been found to have degenerate resistances unless asymmetries are introduced [32, 33]. The switching fields required to achieve these states increases as the element size decreases owing to the larger shape anisotropy energy barrier to reversal.

The approximation of non-interacting single-layer rings does not explain much of the complex behavior. For example, soft layer intermediate states do not tend to be stable over a large field range as can be seen from a variety of published works [3, 34, 35]. The magnetostatic coupling between the layers tends to reverse completely the much softer NiFe layer in order to have an opposite magnetization to the hard layer. Another interesting observation is that the complex DW nucleation patterns allow for 360° DWs to be trapped in rings of certain dimensions [34].

1.3 Device Applications

Device concepts have mainly been developed using more traditional geometries of bars and elliptical disks. There are many devices that utilize ring elements, but the fundamental designs are primarily the same. Beyond the hard disk read head, two predominant areas that patterned GMR elements have found applications in are data

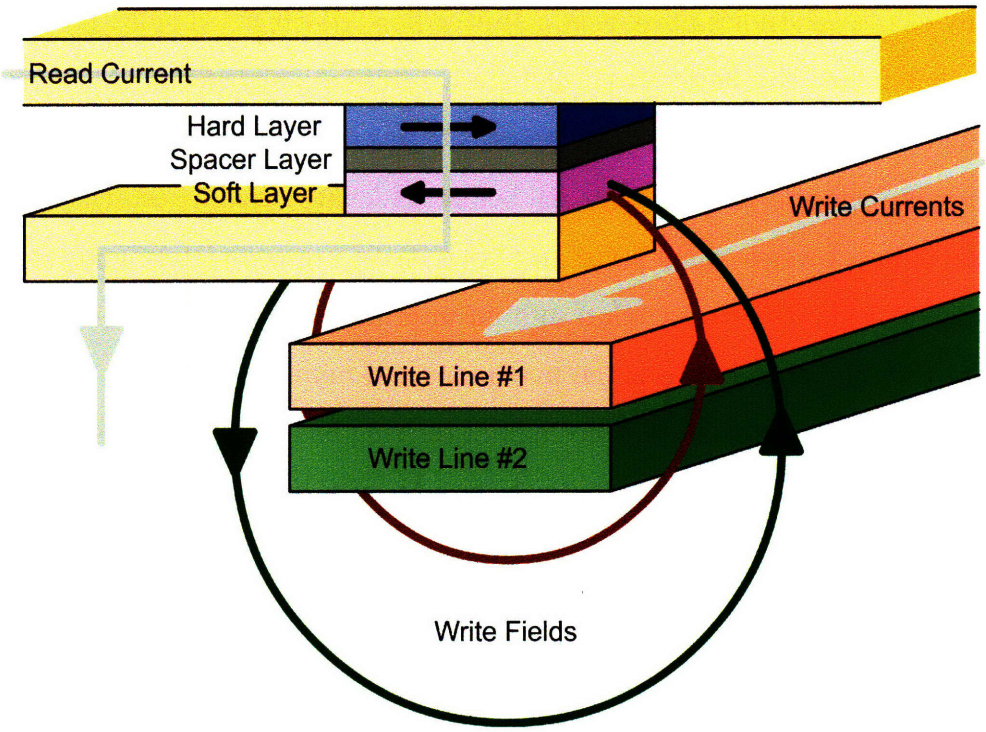

Figure 1-4: A schematic of an MRAM device. MRAMs that change bits using magnetic fields pass currents through the write lines, whereas those using spin transfer torque pass currents along the same path as the read current. Programmable logic gates require two write lines, where each write current represents an input.

storage, and, more recently, computer logic.

1.3.1 Data Storage

Several varieties of magnetic random access memories (MRAMs) have been proposed (Figure 1-4) [36, 37, 38]. GMR-based MRAM uses a hard layer with a constant magnetization direction while the soft layer is changed using applied fields (Figure 1-5a). Current is passed through the magnetic layers to detect whether there is a high resistance state or a low resistance state. Each of these resistance states are thus used as two distinct bits – either a '1' or a '0' (Figure 1-5b).

There are two main methods for switching the soft layer. The first is to use a magnetic field that is generated from a nearby current-carrying wire. However, in an array of elements, all elements by the current-carrying wire will experience the same field and switch. Thus, it is typical to position the elements in a square

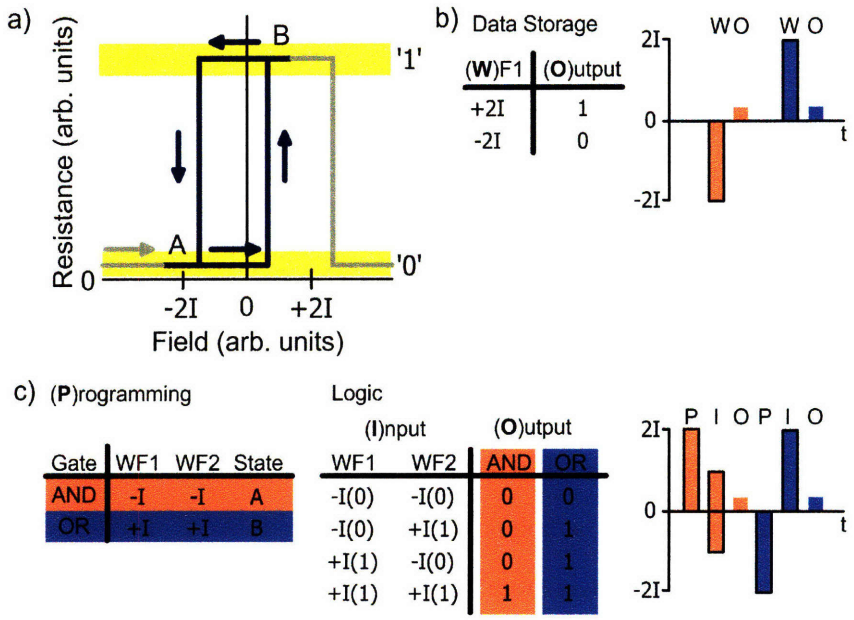

Figure 1-5: a) A magnetic trace where only the soft layer is cycled to be parallel [A] and antiparallel [B] with the hard layer. b) Storage applications only require one write line to set the soft layer into a particular orientation representing different bit states. c) Programmable logic applications require two write lines with programming, input and output steps performed sequentially.

array with perpendicular sets of wires [39]. To address a single element, the two current-carrying wires above an element produce magnetic fields that sum. The second method of switching the soft layer is by exploiting spin-transfer torque [40, 41]. In this scheme, current is passed through part of the element, polarizing electrons in a certain magnetization direction. If the current density is sufficient, the electrons will transfer momentum to the spins in the soft layer and switch it depending on the current direction. For multi-layers that have current-in-plane, the majority of the spin-transfer torque occurs at domain walls.

The appeal of MRAM is in its non-volatility, low power consumption and fast switching times [37]. Moreover, fabrication of the devices can take advantage of the existing semiconductor processing infrastructure. These types of RAM have gained interest with a variety of companies, including Honeywell, Motorola, Freescale, Infineon and IBM, and have been commercially produced by Freescale [38, 42].

1.3.2 Computer Logic

The move to non-volatile and power efficient devices has brought consideration of GMR-based devices as programmable logic gates. The idea was first presented by Shen et al. [43], whereby a magnetoresistive logic element takes current inputs, performs a logic operation and returns a voltage output in sequential steps (Figure 1-5c).

The current inputs are manifested as write lines passing by the magnetic element, which each produce a magnetic field around it. These inputs are defined such that a '0' input state corresponds to a negative field, whereas a '1' input corresponds to a positive field. Depending on the polarity of these two currents, the produced fields can add or cancel. The resultant field interacts with the element and can switch the magnetization of the soft layer. The resistance can be determined with a measurement current at remanence, which yields the output state.

The initial state of the soft layer can be changed prior to the logic operation using a programming step, thereby yielding different outputs for the same inputs. This effectively allows for the element to perform different logic operations that can be set before the input and output phase.

This is different from current computer architecture because there is no need for a clock cycle. Elements can be programmed and accessed at any time without losing their information, allowing potentially more power-efficient computing [6]. Further, several logic operations can be performed using a single magnetoresistive element.

1.4 Thesis Overview

Despite the broad on-going research in magnetic rings, the exact magnetic reversal mechanism is still unknown for a variety of multi-layered rings. The understanding of reversal behaviors is paramount to bridging the gap between individually patterned ring elements and using these elements in devices. Not only does their reliability need to be gauged, but also attributes with which to exploit. This thesis attempts to elucidate the magnetic switching mechanisms in rings that have dimensions which

specifically trap only transverse domain walls.

This thesis follows the below format:

Chapter 2 describes the experimental methods used throughout the thesis.

Chapter 3 focuses on electrically probed PSV elliptical ring devices, including insights into the magnetic reversal mechanism and potential applications of a ring contacted in a symmetric Wheatstone bridge configuration.

Chapter 4 shows how the same magnetic reversal in elliptical rings can be controlled by introducing domain wall nucleation sites and free paths for propagation in a PSV rhombic ring geometry.

Chapter 5 will summarize the key findings of this thesis and give suggestions for future work.

References

[1] G. Binasch, P. Grünberg, F. Saurenbach and W. Zinn, "Enhanced magnetoresistance in layered magnetic structures with antiferromagnetic interlayer exchange," *Phys. Rev. B*, vol. 39, no. 7, pp. 4828-4830, Mar. 1989.

[2] M.N. Baibich, J.M. Broto, A. Fert, F.N. Van Dau, F. Petroff, P. Eitenne, G. Creuzet, A. Friederich and J. Chazelas, "Giant magnetoresistance of (001)Fe/(001)Cr magnetic superlattices," *Phys. Rev. Lett.*, vol. 61, no. 21, pp. 2472-2475, Nov. 1988.

[3] J.R. Childress and R.E. Fontana Jr., "Magnetic recording read head sensor technology," *R. Physique*, vol. 6, no. 9, pp. 997-1012, Nov. 2005.

[4] P.P. Freitas, R. Ferreira, S. Cardoso and F. Cardoso,"Magnetoresistive sensors," *J. Phys. Cond. Mat.*, vol. 19, no. 13, pp. 165221-16542, Apr. 1997.

[5] G.A. Prinz, "Magnetoelectronics," *Science*, vol. 282, no. 5394, pp. 1660-1663, Nov. 1998.

[6] A. Ney, C. Pampuch, R. Koch and K.H. Ploog, "Programmable computing with a single magnetoresistive element," *Nature*, vol. 425, no. 6957, pp. 485-487, Oct. 2003.

[7] A. Wang, "Static magnetic memory: its applications to computers and controlling systems," *ACM Annual Conference Proceedings*, pp. 207-212, 1952.

[8] C.A. Ross, F.J. Castaño, W. Jung, B.G. Ng, I.A. Colin, D. Morecroft, "Magnetism in multi-layer thin film rings," *J. Phys. D: Appl. Phys.*, vol. 41, no. 11, pp. 113002-113007, Jun. 2008.

[9] S.M. Thompson,"The discovery, development and future of GMR: The Nobel Prize 2007," *J. Phys. D: Appl. Phys.*, vol. 41, no. 9, pp. 093001-093021, May 2008.

[10] J.F. Gregg, I. Petej, E. Jouguelet and C. Dennis,"Spin electronics – a review," *J. Phys. D: Appl. Phys.*, vol. 35, no. 18, pp. R121-R155, Sep. 2002.

[11] S.S.P. Parkin,"Systematic variation of the strength and oscillation period of indirect magnetic exchange coupling through the 3d, 4d, and 5d transition metals," *Phys. Rev. Lett.*, vol. 67, no. 25, pp. 3598-3601, Dec. 1991.

[12] T. Shinjo and H. Yamamoto,"Large magnetoresistance of field-induced giant ferrimagnetic multi-layers," *J. Phys. Soc. Jpn.*, vol. 59, pp. 3061-3064, May 1990.

[13] B. Dieny, P. Humbert, V.S. Speriosu, S. Metin, B.A. Gurney, P. Baumgart and H. Lefakis,"Giant magnetoresistance of magnetically soft sandwiches: dependence on temperature and on layer thicknesses," *Phys. Rev. B*, vol. 45, no. 2, pp. 806-813, Jan. 1992.

[14] D.D. Tang, P.K. Wang, V.S. Speriosu, S. Le and K.K. Kung,"Spin-valve RAM cell," *IEEE T. Magn.*, vol. 31, no. 6, pp. 3206-3208, Nov. 1995.

[15] J.G. Zhu and Y. Zheng,"Ultrahigh density vertical magnetoresistive random access memory," *J. Appl. Phys.*, vol. 87, no. 9, pp. 6668-6673, May 2000.

[16] S.P. Li, D. Peyrade, M. Natali, A. Lebib, Y. Chen, U. Ebels, L.D. Buda and K. Ounadjela,"Flux closure structures in cobalt rings," *Phys. Rev. Lett.*, vol. 86, no. 6, pp. 1102-1105, Feb. 2001.

[17] X. Zhu, P. Grütter, V. Metlulshko, Y. Hao, F.J. Castaño, C.A.Ross, B. Ilic and H.I. Smith,"Construction of hysteresis loops of single domain elements and coupled permalloy ring arrays by magnetic force microscopy," *J. Appl. Phys.*, vol. 93, no. 10, pp. 8540-8452, May 2003.

[18] J. Rothman, M. Kläui, L. Lopez-Diaz, C.A.F. Vaz, A. Bleloch, J.A.C. Bland, Z. Cui and R. Speaks,"Observation of a bi-domain state and nucleation free switching in mesoscopic ring magnets," *Phys. Rev. Lett.*, vol. 86, no. 6, pp. 1098-1101, Feb. 2001.

[19] M.M. Miller and G.A. Prinz and S.F. Cheng and S. Bounnak,"Detection of a micron-sized magnetic sphere using a ring-shaped anisotropic magnetoresistance-based sensor: A model for a magnetoresistance-based biosensor," *Appl. Phys. Lett.*, vol. 81, no. 12, pp. 2211-2213, Sep. 2002.

[20] T. Kimura and Y. Otani,"Magnetization of a single magnetic ring detected by nonlocal spin valve measurement," *J. Appl. Phys.*, vol. 101, no. 12, pp. 126102, Jun. 2007.

[21] M. Kläui, J. Rothman, L. Lopez-Diaz, C.A.F. Vaz, J.A.C. Bland and Z. Cui, "Vortex circulation control in mesoscopic ring magnets," *Appl. Phys. Lett.*, vol. 78, no. 21, pp. 3268-3270, May 2001.

[22] Y.G. Yoo, M. Kläui, C.A.F. Vaz, L.J. Heyderman and J.A.C. Bland, "Switching field phase diagram of Co nanoring magnets," *Appl. Phys. Lett.*, vol. 82, no. 15, pp. 2470-2472, Apr. 2003.

[23] R.D. McMichael and M.J. Donahue,"Head to head domain wall structures in thin magnetic strips," *IEEE T. Magn.*, vol. 33, no. 5, pp. 4167-4169, Sep. 1997.

[24] M. Kläui, C.A.F Vaz, J.A.C. Bland, L.J. Heyderman, F. Nolting, A. Pavlovska, E. Bauer, S. Cherifi, S. Heun and A. Locatelli, "Head-to-head domain-wall phase diagram in mesoscopic ring magnets," *Appl. Phys. Lett.*, vol. 85, no. 23, pp. 5637-5639, Dec. 2004.

[25] L. Lopez-Diaz, J. Rothman, M. Kläui, and J.A.C. Bland, "Computational study of first magnetization curves in small rings," *IEEE T. Magn.*, vol. 36, no. 5, pp. 3155-3157, Sep. 2000.

[26] L. Lopez-Diaz, J. Rothman, M. Kläui, and J.A.C. Bland, "Vortex formation in magnetic narrow rings: The role of magneto-crystalline anisotropy," *J. Appl. Phys.*, vol. 89, no. 11, pp. 7579-7581, Jun. 2001.

[27] M. Kläui, C.A.F Vaz, L. Lopez-Diaz and J.A.C. Bland, "Vortex formation in narrow ferromagnetic rings," *J. Phys.: Condens. Matter*, vol. 15, pp. R985-R1023, 2003.

[28] F.J. Castaño, D. Morecroft, W. Jung and C.A. Ross, "Spin-dependent scattering in multi-layered magnetic rings," *Phys. Rev. Lett.*, vol. 95, no. 13, pp. 137201, Sep. 2004.

[29] H.X. Wei, F.Q. Zhu, X.F. Han, Z.C. Wen and C.L. Chien, "Current-induced multiple spin structures in 100 nm ring magnetic tunnel junctions," *Phys. Rev. B*, vol. 77, no. 22, pp. 224432, Jun. 2008.

[30] T. Miyawaki, M. Kohda, A. Fujita and J. Nitta, "Control of interlayer magnetostatic coupling in submicron-sized Fe/Au/Fe rings," *Appl. Phys. Lett.*, vol. 92, no. 3, pp. 032502, Jan. 2008.

[31] Z.C. Wen, H.X. Wei and X.F. Han, "Patterned nanoring magnetic tunnel junctions," *Appl. Phys. Lett.*, vol. 91, no. 12, pp. 122511, Jan. 2008.

[32] T.J. Hayward, J. Llandro, R.B. Balsod, J.A.C. Bland, F.J. Castaño, D. Morecroft and C.A. Ross, "Reading and writing of vortex circulation in pseudo-spin-valve ring devices," *Appl. Phys. Lett.*, vol. 89, no. 11, pp. 112510, Sep. 2006.

[33] X. Zhu and J.G. Zhu, "A vertical MRAM free of write disturbance," *IEEE T. Magn.*, vol. 39, no. 5, pp. 2854-2856, Sep. 2003.

[34] F.J. Castaño, C.A. Ross, C. Frandsen, A. Eilez, D. Gil, H.I. Smith, M. Redjdal and F.B. Humphrey, "Metastable states in magnetic nanorings," *Phys. Rev. B*, vol. 67, no. 18, pp. 184425, May 2003.

[35] F.J. Castaño, C.A.Ross, A. Eilez, W. Jung, and C. Frandsen, "Magnetic configurations in 160520-nm-diameter ferromagnetic rings," *Phys. Rev. B*, vol. 69, no. 14, pp. 144421, Apr. 2004.

[36] J.M. Daughton, A.V. Phom, R.T. Fayfield and C.H. Smith, "Applications of spin dependent transport materials," *J. Phys. D*, vol. 32, no. 1, pp. R169-R177, Sep. 1999.

[37] W.J. Gallagher and S.S.P. Parkin, "Development of the magnetic tunnel junction MRAM at IBM: from first junctions to a 16-Mb MRAM demonstrator chip," *IBM J. Res. Dev.*, vol. 50, no. 1, pp. 5-23, Jan. 2006.

[38] C. Chappert, A. Fert and F.N. Van Dau, "The emergence of spin electronics in data storage," *Nat. Mat.*, vol. 6, no. 11, pp. 813-823, Nov. 2007.

[39] R. E. Scheuerlein, "Magneto-resistive IC memory limitations and architecture implications," *IEEE International Nonvolatile Memory Technology Conference Proceedings*, pp. 47-50, 1998.

[40] J.A. Katine and E.E. Fullerton, "Device implications of spin-transfer torques," *J. Magn. Magn. Mat.*, vol. 320, no. 7, pp. 1217-1226, Apr. 2008.

[41] T. Kawahara, R. Takemura, K. Miura, J. Hayakawa, S. Ikeda, Y.M. Lee, R. Sasaki, Y. Goto, K. Ito, T. Meguro, F. Matsukura, H. Takahashi, H. Matsuoka and H. Ohno, "2 Mb SPRAM (SPin-Transfer Torque RAM) with bit-by-bit bi-directional current write and parallelizing-direction current read," *IEEE J. Solid-St. Circ.*, vol. 43, no. 1, pp. 109-120, Jan. 2008.

[42] T.W. Andre, J.J Nahas, C.K. Subramanian, B.J. Garni, H.S. Lin, A. Omair and W.L. Martino Jr., "A 4-Mb 0.18μm 1T1MTJ toggle MRAM with balanced three input sensing scheme and locally mirrored unidirectional write drivers," *IEEE J. Solid-St. Circ.*, vol. 40, no. 1, pp. 301- 309, Jan. 2005.

[43] J. Shen, "Logic devices and circuits based on giant magnetoresistance," *IEEE T. Magn.*, vol. 33, no. 6, pp. 4492-4497, Nov. 1997.

Chapter 2

Experimental Methods

This chapter covers the details of the device fabrication and characterization that were used throughout the thesis. It begins with the magnetic thin films that were optimized for high GMR ratios, the patterning of the film into a device, and the subsequent electrical measurements of a device under a magnetic field. Micromagnetic simulations were run concurrently in order to gain insights into the switching mechanisms underlying electrical measurements.

2.1 Fabrication

2.1.1 PSV Film Deposition

PSV multi-layer stacks investigated throughout this thesis comprised solely of polycrystalline NiFe/Cu/Co with typical grain sizes of approximately 15nm. Unless otherwise specified, the exact magnetic stack was NiFe(6)/Cu(4)/Co(5)/Au(4), where the numbers refer to the nominal film thickness in nm. The substrate was a prime Si(100) wafer with 50nm of thermal oxide. This thickness was chosen so as not to build up large amounts of charge from electron beams, as well as to provide adequate electrical insulation from and heat dissipation to the Si.

The amorphous nature of thermal oxide induced the growth of polycrystalline films above it. The Co is assumed to have grown in hexagonal close packed crys-

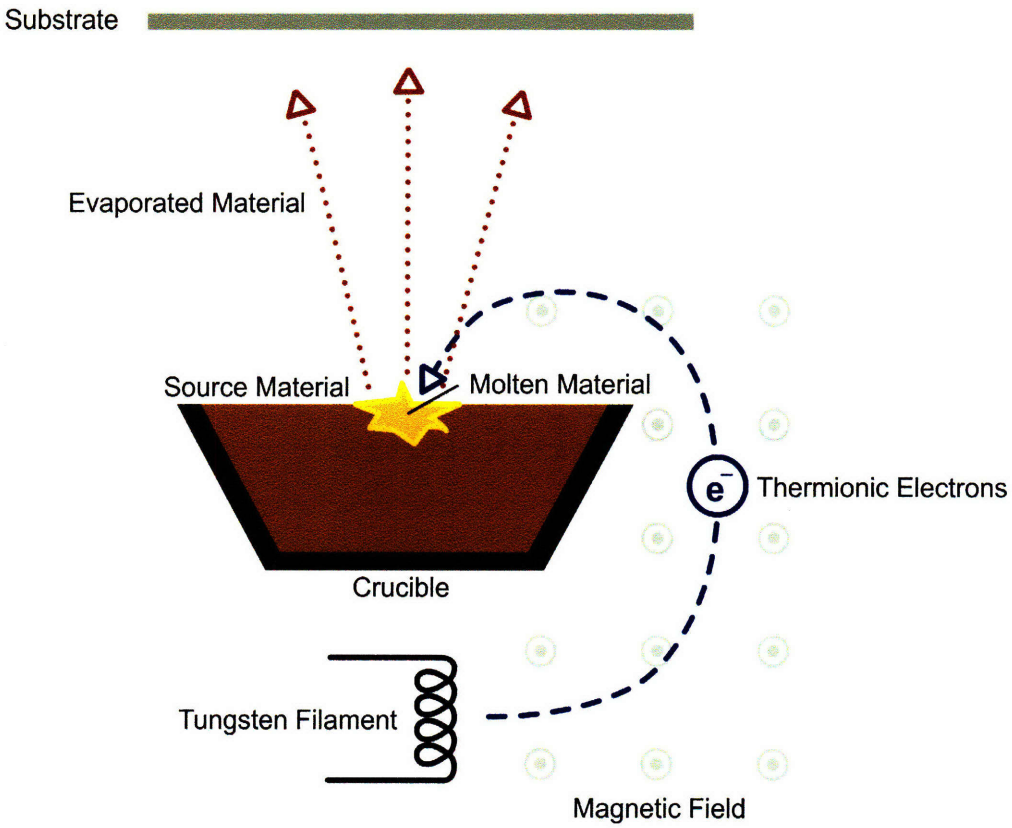

Figure 2-1: A schematic of e-beam evaporation.

tal structure grains for room temperature depositions [1]. Although Co has a large magnetocrystalline anisotropy, the random distribution of crystallographic orientations among grains results in magnetically isotropic films. The polycrystalline NiFe grows in an face-center cubic crystal structure and has a small magnetocrystalline anisotropy contribution [2].

The Au capping layer was used to reduce the oxidation of the Co layer, as well as to improve Ohmic contact. Although part of the current is shunted through this conductive layer, the shunting is not significant enough to mask the magnetoresistive response. The PSV stacks were made either entirely with electron-beam (e-beam) evaporation or with a combination of DC-triode magnetron and ion beam sputtering.

E-beam evaporation operates by directing a beam of thermionic electrons from a tungsten filament onto a source material (Figure 2-1). The beam of electrons is able to locally produce high temperatures, boil the source material and induce the material to evaporate. As the evaporated atoms arrive at the substrate, they condense to

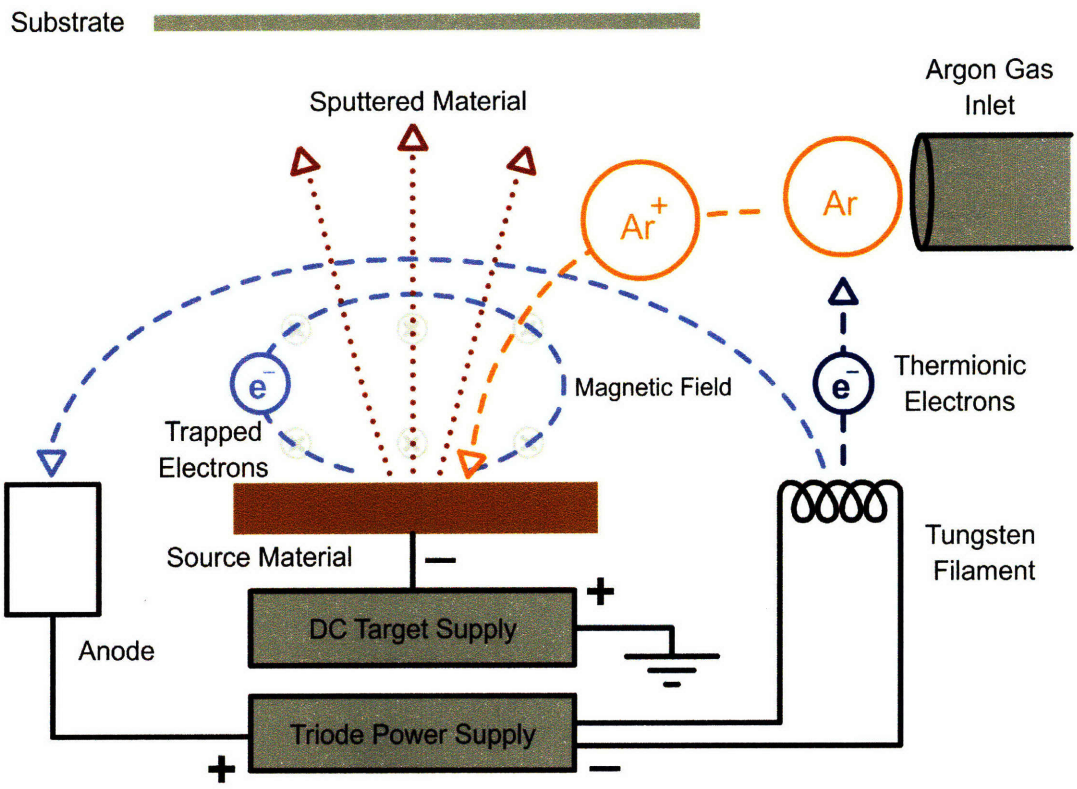

Figure 2-2: A schematic of DC-triode magnetron sputtering.

form a film. These films have the potential to be very pure since evaporation occurs in high vacuums without the presence of a gas. Deposition was performed at room temperature in pressures on the order of 10^{-6}Torr, which is a relatively high pressure for deposition.

PSV stacks were also deposited using a combination of DC-triode magnetron and ion-beam sputtering in an ultra-high vacuum chamber. The sputtering chamber maintained a base vacuum pressure of between 5×10^{-8}Torr to 5×10^{-10}Torr.

The DC-triode magnetron sputtering utilizes electrons ejected from a tungsten filament source that travel toward an anode (Figure 2-2). Ar gas that is fed by the electron source is ionized, creating a plasma of positively charged Ar+ ions. The target metal is then biased with a DC voltage between -100V and -200V so that the Ar+ ions are accelerated toward the source, transfer energy to the surface and physically sputter off the source metal atoms. The sputtered atoms travel toward the substrate and adsorb onto the surface. Secondary electrons that are emitted during

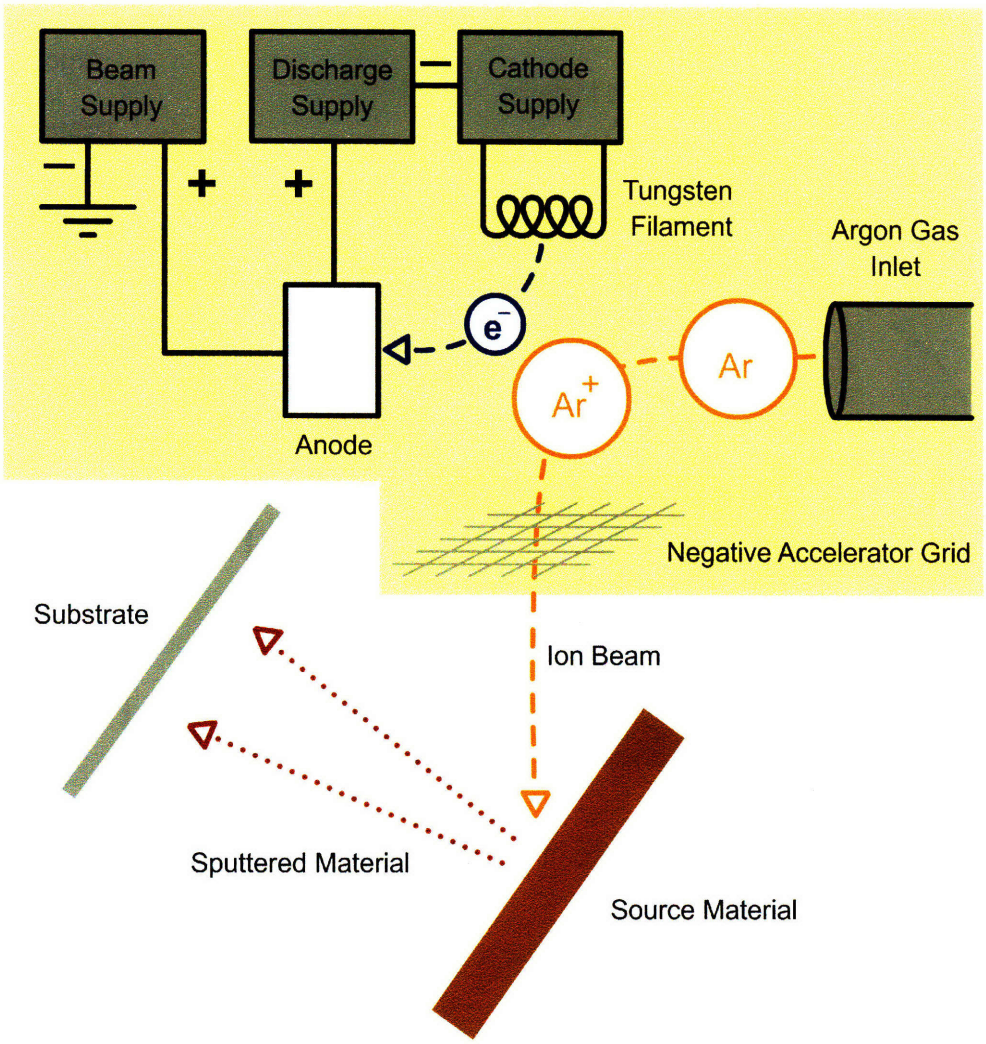

Figure 2-3: A schematic of ion beam sputtering.

sputtering are redirected back to the plasma with permanent magnets to reionize neutral Ar atoms. This efficiency allows the use of low working pressures, which decreases gas and plasma contamination and create high purity films. Film growth was carried out with a plasma voltage of 60V , plasma current of 2A , and bias power of 100W at an Ar pressure of 1mTorr. Metal targets of 3" diameter were used including NiFe, Cu, Co, Ta and Au.

Ion beam sputtering also uses Ar+ ions to bombard a target, with the difference that Ar+ ions are generated in an ionization chamber away from the target (Figure 2-3). Electrons are emitted from a tungsten filament and ionize Ar gas flowing by the cathode. A negatively biased accelerator grid moves ions out of the ionization chamber

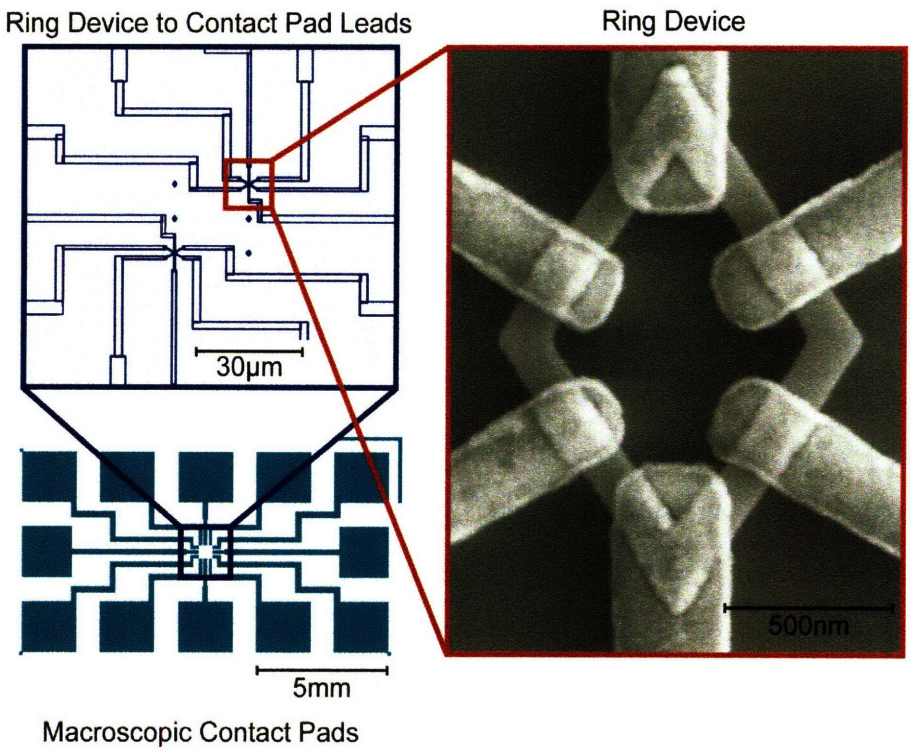

Figure 2-4: A schematic of chips used to electrically probe PSV ring devices. The macroscopic contact pads (lower left) were fabricated with optical lithography, while the magnetic ring (right) and the electrical probes to the ring (upper left) were fabricated with e-beam lithography.

toward a metal target, sputtering the metal onto the substrate. Since the plasma is generated away from the source metal, the deposition rate is much slower than DC-triode magnetron sputtering, but films are free from damage or contamination caused by a plasma [3, 4]. Also, the deposition pressure can be maintained much lower since the ionization of the Ar occurs in a small, confined chamber. Ultimately, fewer collisions allow ion beam sputtering to be highly directional when compared to other sputtering methods. Deposition occurred at pressures of 4.0×10^{-5}Torr . The beam voltage was 1000V , the acceleration voltage was 250V and the discharge voltage was 40V. The cathode current was varied to maintain a beam current of 35mA.

2.1.2 Electrical Device Fabrication

The fabrication process was to first create macroscopic contact pads, then create the magnetic ring structure, and finally connect the ring to the contact pads (Figure 2-4).

Photolithography and lift-off processing were used to define the macroscopic contact pads (Figure 2-5). 1μm of S1813 photoresist (Shipley) was spun onto an oxidized wafer and baked on a hot plate at 90°C for 2mins to drive out the solvent. The resist was then exposed with a wide-spectrum Hg lamp (Tamarack ELHG) and developed in 352 (Shipley) developer for 60s before rinsing with deionized water. The duration of the exposure was calibrated with a fixed developing time. After features had been defined in the resist, a Ti(5)/Au(45) was deposited using e-beam evaporation. Ti served as an adhesion layer between the Au and oxidized Si surface. The film was lifted-off using 1-methyl-2-pyrrolidone (NMP) (JT Baker) with a solution temperature of approximately 95°C for 5mins, while the beaker containing the sample and NMP was agitated by hand. The beaker was then placed in a 40kHz sonication bath for 30s to encourage the lift-off process by increasing the exposure of NMP to the photoresist and by breaking up free standing metal or thin sidewall coatings. The NMP was changed and the sample soaked in hot NMP for another 5mins with agitation before another sonication of 30s. The sample was rinsed with isopropyl alcohol (IPA) and dried with nitrogen gas.

The ring pattern was written in the middle of the macroscopic contacts using e-beam lithography. 145nm of 950kMW PMMA in Anisole (Microchem) was spun onto the wafer and baked in a flow-oven at 155°C for 45mins in order to ensure uniform solvent removal. The resist was exposed using scanning e-beam lithography (Raith 150) at 10kV with a 6mm working distance and a 20μm aperture size. The dose was optimized for every size ring using a constant developing time of 90s in 3:1 IPA:methyl isobutyl ketone (MIBK). Rings were written by forcing the position of the beam to follow the path of a ring rather than allowing the e-beam to raster the shapes in a Manhattan geometry. This created symmetric shapes with a better correlation between the intended shapes and the fabricated shapes.

Samples were then developed in 3:1 IPA:MIBK for 90s, and the PSV film deposited on it. The film was lifted-off using hot NMP for 5mins as before, sonicated in NMP for 30s, rinsed with IPA and dried using nitrogen. The quality of the lift-off was primarily determined by the type of film deposition, since each deposit with a different level

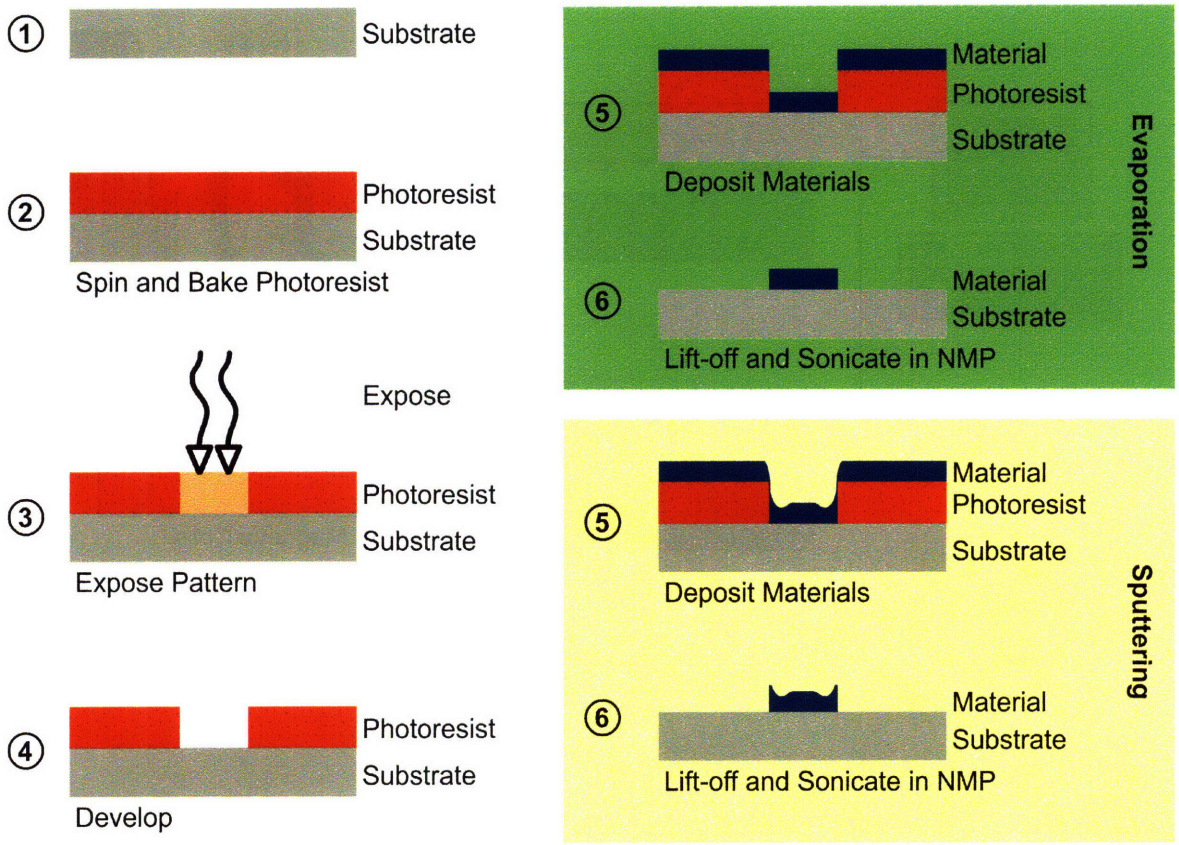

Figure 2-5: A schematic of the lift-off process used to define patterns for the metal layers. The subtle difference between directional films obtained with e-beam evaporation and ion beam sputtering (right top) as opposed to slightly more conformal films obtained with DC-magnetron sputtering that produces "crowning" (right bottom).

of directionality. DC-triode magnetron sputtering tended to more conformal and less directional than both ion beam sputtering and e-beam evaporation [5]. Conformal films produce a characteristic "crowning" effect where the film portion that partially coats the sidewalls remains after lift-off (Figure 2-5). The crowning is not thought to significantly change the magnetic behavior of elements, but does make Ohmic contact with electrodes more difficult.

The contacts between the magnetic rings and the optical contact pads were then patterned. PMMA was spun to 165nm and baked in a flow oven as before. E-beam lithography was used again to define the electrical contacts in a similar manner to the ring devices.

After developing for 100s, the substrate surface was cleaned from organic residue with 5s of in situ ion milling at 2×10^{-4}Torr using 500V beam voltage, 100V

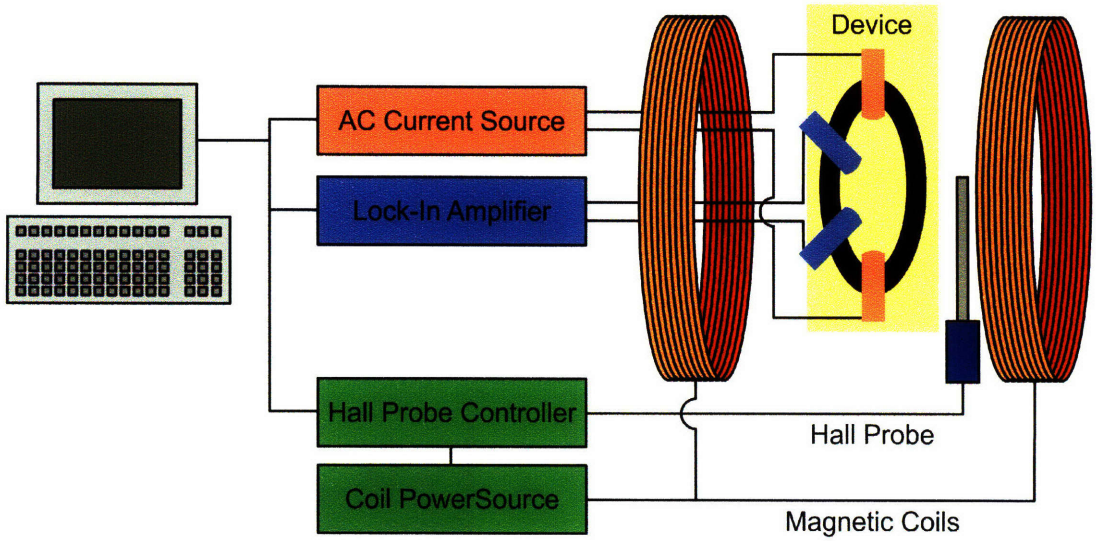

Figure 2-6: A schematic of the magnetoresistance measurement setup.

accelerator voltage, 40V discharge voltage and 5A neutralizer current. 5mA beam current was maintained by modulating the cathode current. It is believed that the ion milling step also aids in smoothing the surface of the ring, which improves the Ohmic contact. Without breaking vacuum, a Ta(2)/Cu(90)/Au(20) stack was deposited to form the electrodes. The very thin Ta is used as an adhesion layer. An ion milled smoothed and cleaned surface as well as a very thin Ta layer were found to significantly increase the yield of Ohmic contacts between the magnetic ring and the metal electrodes.

Cu formed the bulk of the contacts since it has a good conductivity. Cu was found to be superior to Au since it is more tolerant of high current densities before melting or undergoing electromigration. However, Au was used as a capping layer in order to reduce the oxidation of the Cu electrode. After lifting off in hot NMP, a very short 2s sonication was performed. The device was then RF-sputtered with 50nm of SiO_2 using an angled deposition while rotating the substrate. This thin layer of oxide effectively coated the devices and the sidewalls, acting as an oxidation passivation layer that was thin enough to allow heat dissipation.

2.2 Magnetoresistance Measurements

Electrical measurements were performed under applied magnetic fields (Figure 2-6). Chips were mounted in a grounded metal cup to reduce electrical noise. Contact pads were contacted with Au-Be round-tipped pogo pins that were wired to coaxial jacks, which fed the current inputs and voltage outputs. An AC current source (Keithley 6221) provided the continuous sine wave measurement current that maintained an RMS amplitude of 10μA and a frequency of 1kHz. A lock-in amplifier (SRS SR830) measured the differential voltage between two connected leads, and the voltage reading taken at a phase angle of less than 1°.

Care needed to be taken to ensure that the MR setup was properly grounded to reduce electrostatic discharge. Also, the compliance voltage limit was never allowed to be over 300mV, since it was found that allowing voltages greater than that would melt chips, or cause localized heating that could constrict ring segments.

The magnetic field was provided by large iron-core magnetic coils using a 100A/50V power supply that was controlled by a Hall probe monitor/controller (LakeShore 420). This setup used a feedback loop to adjust the coil current with an accuracy of 0.01A , or roughly 0.7Oe. The Hall probe was placed in line with the mounted sample and the field assumed to be representative of the field through the device. Saturation using this system is defined as passing 60A and -60A through the coils for positive and negative saturation respectively. That current roughly corresponds with a field magnitude of 5000Oe. The electrical measurements and the regulation of the magnetic field were controlled by computer.

2.3 Micromagnetic Simulations

2.3.1 OOMMF

Micromagnetic simulations were performed using the Object Oriented Micromagnetic Framework (OOMMF) provided by the National Institute of Standards and Technology (NIST) [6]. Materials properties, magnetic interaction parameters, geometries,

and Zeeman energies were user-input. The simulations gave insight into possible energetically favorable magnetic configurations of the devices by using a Landau Lifshitz Gilbert (LLG) differential equation solver that relaxed 3D spins on a mesh of square cells.

The LLG equation takes the form of:

$$\frac{d\mathbf{M}}{dt} = -|\overline{\gamma}|\mathbf{M} \times \mathbf{H}_{eff} - \frac{|\overline{\gamma}|\alpha}{\mathbf{M}_s}\mathbf{M} \times (\mathbf{M} \times \mathbf{H}_{eff}) \tag{2.1}$$

where $\mathbf{M}$ is the magnetization, $\mathbf{H}_{\text{eff}}$ is the effective field, γ is the Gilbert gyromagnetic ratio and α is the damping constant. In essence, the LLG equation relates the change of any given magnetic moment to the influence of the demagnetization field created from different magnetic field components – such as Zeeman, exchange, magnetostatic, shape anisotropy – in addition to a damping term for moment precession.

Geometries of the samples were defined by either importing bitmaps of computer-generated shapes or importing scanning electron microscopy (SEM) images, and then discretizing the images from pixels into the simulation mesh. The computer-generated shapes had an exact pixel to square mesh mapping, and were used to identify typical magnetic reversal mechanisms in the absence of fabrication shape defects. On the other hand, SEM images of fabricated devices were captured in resolutions of 512x512 pixels. Local variations of geometry and roughness inherent in device fabrication were better captured in these simulations, but these images also created artificial edges due to the coarse SEM image pixel resolution relative to the mesh size.

The square mesh sizes used were either 4x4x4nm, or 5x5x4nm to be on the order of the exchange length of permalloy and cobalt which are between 3nm and 8nm [7]. Since the simulation mesh needed to be of a uniform size, it was not computationally practical to simulate the exact thicknesses of the magnetic stacks, but rather thicknesses that were multiples of the z-dimension of the meshes (4nm). It has been shown in literature that experimental samples of 4nm layer thicknesses and the thicknesses of the experimental multi-layers used throughout this thesis should exhibit the same similar switching mechanisms but at different switching fields [8]. Thus,

Constant	Value
$A^{NiFe-NiFe}$	$13 \times 10^{-12} \frac{J}{m}$
A^{Co-Co}	$30 \times 10^{-12} \frac{J}{m}$
$A^{NiFe-Co}$	$30 \times 10^{-12} \frac{J}{m}$
K_1^{NiFe}	$520 \times 10^3 \frac{J}{m^3}$
K_1^{Co}	$500 \frac{J}{m^3}$
M_s^{NiFe}	$860 \times 10^3 \frac{A}{m}$
M_s^{Co}	$1400 \times 10^3 \frac{A}{m}$
α	0.5
$\overline{\gamma}$	$2.21 \times 10^5 \frac{m}{As}$

Table 2.1: Constants used throughout all OOMMF simulations.

throughout the thesis, experimental stacks of NiFe(6)/Cu(4)/Co(5) are modeled as NiFe(4)/Cu(4)/Co(4).

Anisotropy vectors were assumed to be of constant magnitude but in random directions in the plane of the device in order to simulate the polycrystallinity of films. The magnitudes of the exchange stiffness (A), the first-order anisotropy constant (K_1) and the saturation magnetization (M_S) were assumed to be consistent with literature and constant among the samples. The constants used throughout all of the simulations are listed in Table 2.1. An example of the simulation script can be found in Appendix A.

2.3.2 Magnetoresistance Calculations

Magnetoresistance of the multi-layers was calculated by assuming that only cells directly above and below a given spacer cell contributed to the resistance of that spacer cell for electrons flowing through it. That is to say, the NiFe and Co magnetization vectors with the same in-plane coordinate (x,y) in simulation space were compared

to define a magnetoresistance magnitude. As a model, only the angular comparison of the NiFe and Co layers were used:

$$r_{x,y} = \frac{1}{2}(1 - cos\theta_{x,y}) = \frac{1}{2}\left(1 - \frac{\mathbf{M}_{NiFe} \cdot \mathbf{M}_{Co}}{|\mathbf{M}_{NiFe}||\mathbf{M}_{Co}|}\right) \tag{2.2}$$

In reality, electrons undergo spin-dependent scattering with not only magnetic moments directly above and below its path, but also with adjacent moments. As an approximation to average this effect, all of the small resistance cells in a particular branch are summed to yield the overall resistance of a given segment of device:

$$R_{segment} = \frac{\sum_{x,y} r_{x,y}}{N_{allcells}} \tag{2.3}$$

This assumption is expected to hold true for current flow also, since any localized low-resistance areas will conduct more current flow, heat slightly, and distribute the current through the remainder of the ring segment.

These calculations yield arbitrary units of resistance, but are useful to compare trends in the magnetization reversal, and the relative magnitudes of resistance changes. Thus, comparisons to experimental data are performed by scaling the maximum and minimum calculated values to the maximum and minimum experimental values. In some cases, specific portions of the magnetic devices were omitted in the calculations to correspond with electrode contact areas. In these omitted areas there should be no current flow, and thus no influence to the overall resistance.

References

[1] H.T. Shi and D. Lederman, "Surface smoothing and crystalline reorientation in thin cobalt films," *Phys. Rev. B*, vol. 58, no. 4, pp. R1778-R1781. Jul. 1998.

[2] S. Narishige, K. Mitsuoka and Y. Sugita, "Crystal structure and magnetic properties of permalloy films sputtered by mixed Ar-N_2 Gases," *IEEE T. Magn.*, vol. 28, no. 2, pp. 990-993. Mar. 1992.

[3] Y. Miyamoto, T. Yoshitani and M. Naoe, "Investigations of GMR characteristics and crystal structures for $Ni_{81}Fe_{19}$/Cu multi-layers with Ar ion bombardment on interfaces," *IEEE T. Magn.*, vol. 32, no. 5, pp. 4719-4721, Sept. 1996.

[4] J.M. Slaughter, E.Y. Chen and S. Tehrani, "Magnetoresistance of ion-beam deposited Co/Cu/Co and NiFe/Co/Cu/Co/NiFe spin valves," *J. Appl. Phys.*, vol. 85, no. 8, pp. 4451-4453, Apr. 1999.

[5] C. Redondo, S. Moralejo, F. Castaño, W. Lee, K. Nielsch, C.A. Ross and F.J. Castaño, "Additive patterning of ion-beam-sputtered non-conformal $Ni_{80}Fe_{20}$ and $Co_{70}Fe_{30}$ magnetic films," *Nanotechnology*, vol. 17, no. 8, pp. 20402045, Mar. 2006.

[6] M. Donahue and D. Porter. "The Object Oriented MicroMagnetic Framework (OOMMF) project at ITL/NIST," *The National Institute of Science and Technology*. Available: http://math.nist.gov/oommf/. [Accessed: August 15, 2008]

[7] R.C. O'Handley, *Modern magnetic materials*, New York: John Wiley and Sons, 2000, pp. 296.

[8] F.J. Castaño, C.A. Ross, C. Frandsen, A. Eilez, D. Gil, H.I. Smith, M. Redjdal and F.B. Humphrey, "Metastable states in magnetic nanorings," *Phys. Rev. B*, vol. 67, no. 18, pp. 184425, May 2003.

Chapter 3

Elliptical Magnetic Rings

Elliptical magnetic rings are convenient geometries since there are many stable intermediate states to exploit for magnetoelectronic applications. Elliptical rings are advantageous over completely symmetric circular configurations since definite easy and hard axes allow for preferential positioning of DWs and the engineering of switching fields. However, magnetostatic coupling in magnetic multi-layers, and intricate balances of competing energies introduce a great level of complexity that make the understanding of the magnetic reversal behavior non-trivial. In this chapter, experimental electrical measurements are described and compared with micromagnetic simulations. The Wheatstone bridge contact configuration is found to yield new information on magnetic reversals. In particular, the symmetric Wheatstone bridge is explored and evaluated as a device for data storage and logic applications.

3.1 Electrical Contact Configurations

To probe a PSV device, an electrical current is passed between two probes to detect the relative orientations of the magnetic layers. Annular structures allow many different contact variations where each variation measures slightly different attributes of a ring. The two main types of contacts are 2-point and 4-point methods (Figure 3-1).

2-point contacts have the benefit that the contacts can be large for a given ring

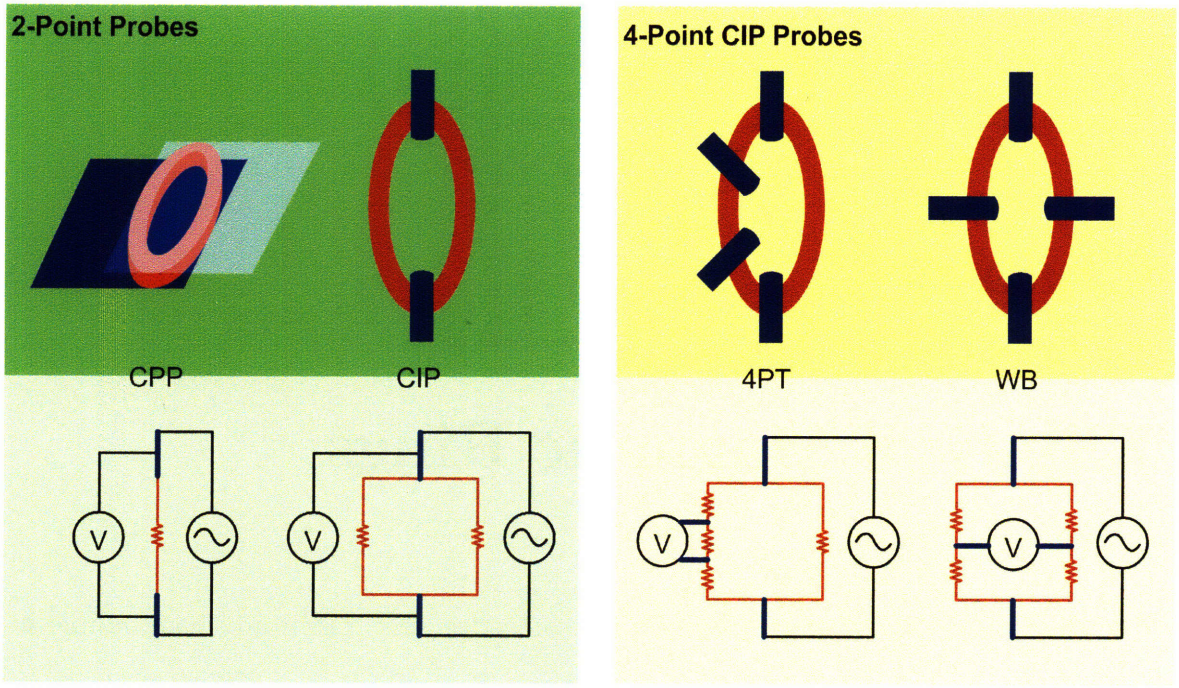

Figure 3-1: The top row of schematics shows the different types of electrical contacts that are often made in device applications. From left to right, they are two-point CPP, two-point CIP, 4PT CIP and WB CIP. The second row illustrates the equivalent circuit diagrams of the schematics above them.

size, and are thus preferred for scaling down the size of the rings for high densities. These types of probes measure the overall behavior of a ring, either with a current-perpendicular-to-plane (CPP) measurement where the ring is treated as a single resistive unit, or a current-in-plane (CIP) measurement where the two sections in between the contacts are measured in parallel.

On the other hand, 4-point CIP configurations are ideal to obtain insights into the magnetization reversal of rings since additional information from specific sections of the ring can be determined. The two main types of 4-point contacts will be referred to in this thesis as the standard four-point resistance measurement (4PT) and the Wheatstone bridge differential voltage measurement (WB).

3.1.1 4-Point (4PT) Electrical Measurements

4PT measurements consist of two current probes that are separated by two voltage probes in the same current path. This is one of the standard methods of measuring

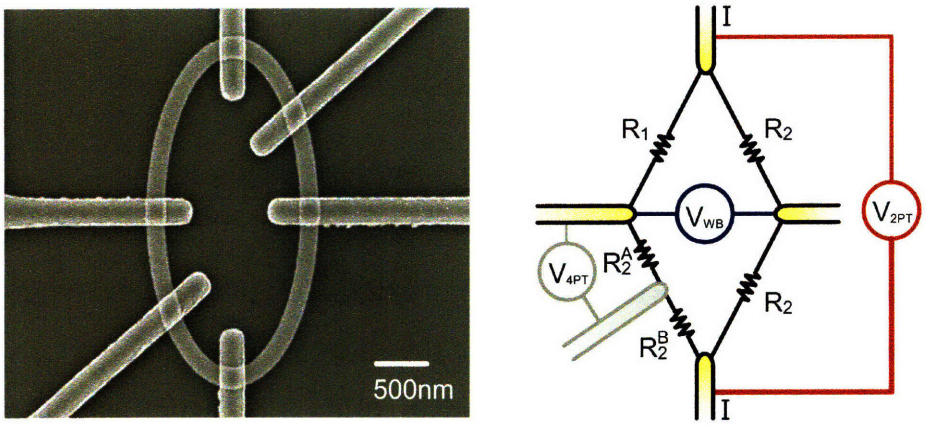

Figure 3-2: A scanning electron micrograph of a 4μm ring with a 2:1 aspect ratio and 220nm linewidth (left), and a circuit diagram illustrating different CIP configurations (right).

the resistivity of bulk films since the contact resistances of the current probes are not measured [1]. Similarly in rings, 4-point electrical contacts are placed on one side of the ring, where two current leads are separated by two voltage probes. Although only a small segment lies between the voltage probes, the electrical response represents the magnetoresistance in the entire ring since the measuring current splits into the two halves of the ring.

It is useful to first describe the measured voltage from a 2PT measurement, using notation in Figure 3-2:

$$V_{2PT} = I_S \frac{\left(R_1 + R_2^A + R_2^B\right)(R_3 + R_4)}{(R_1 + R_2^A + R_2^B + R_3 + R_4)} \tag{3.1}$$

In moving to a 4PT measurement, the potential difference measured by two voltage probes is:

$$V_{4PT} = \frac{R_2^A}{R_1 + R_2^A + R_2^B} V_{2PT} + C \tag{3.2}$$

To obtain an effective resistance value, the current of the entire ring, I_S, is considered for convenience despite the fact that the current between the leads is only a fraction of the source current:

$$R_{4PT} = \frac{V_{4PT}}{I_S} \tag{3.3}$$

The effective resistance is therefore not a true "magnetoresistance" measurement, but rather a probe of the magnetoresistive state through a circuit analysis. That is to say, the contribution of the ring segment between the voltage probes is superimposed onto the 2PT magnetoresistive response of the entire ring.

This 4PT contribution can be lessened by using a configuration where current electrodes are diametrically opposite to each other along the easy axis, and voltage probes are far from each other. As long as external magnetic fields are applied either along the easy or hard axes, the half rings defined by the current leads will switch uniformly. This allows the ratio that scales V_{2PT} in Equation 3.2 to be constant for any equilibrium magnetic state. As such, 4PT resistance values are reproducible from device to device provided that fabrication defects do not allow the segment captured between the voltage leads to nucleate or pin DWs. For these reasons, relative resistance metrics, such as the GMR ratio, are almost identical between the 4PT CIP and 2PT CIP measurements, whereas resistance magnitudes are not.

A 4μm ring with 2:1 aspect ratio and 220nm linewidth was electrically measured as a function of applied field (Figure 3-3). Upon reversing the field from saturation, there are five stages of magnetic reversal:

[A] At saturation, there is a low baseline resistance indicating that the soft and hard layers have magnetizations that are highly parallel.

[B] At 30Oe, there is a jump to an intermediate resistance state. The magnitude of this intermediate state is observed to be less than half of the maximum resistance when reversing from negative saturation, and just greater than half of the maximum when reversing from positive saturation.

[C] At 50Oe, there is a plateau with a maximum resistance value indicating that the soft and hard layers have magnetizations that are highly anti-parallel.

[D] At 190Oe, the resistance drops to an intermediate value that is approximately

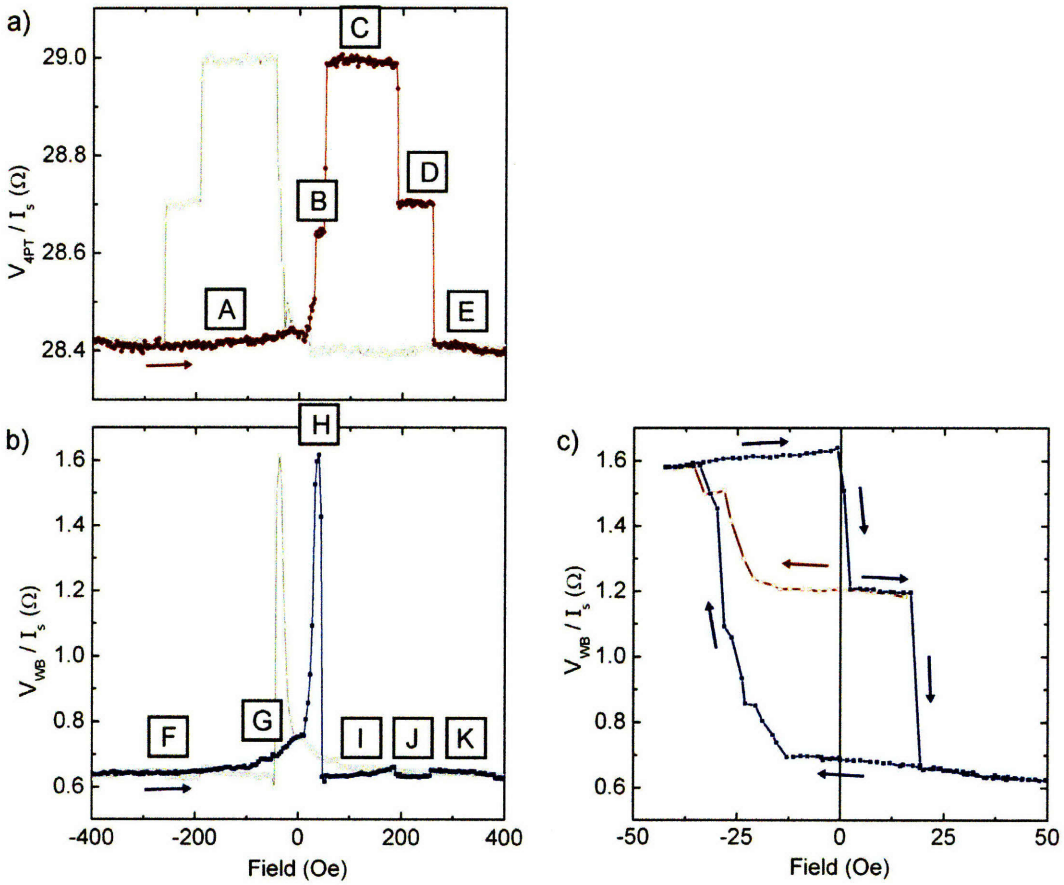

Figure 3-3: The resistance versus field behavior of a 4μm ring with a 2:1 aspect ratio and 220nm linewidth from saturation from a) the 4PT and b) WB (bottom) contact configurations. c) The WB resistance versus field behavior of the same ellipse cycling at various lower fields after positive saturation.

half of the maximum. This half value is the same from both saturations, and indicates that half of the ring has parallel magnetizations while half of the ring has antiparallel magnetizations.

[E] At 260Oe, the resistance drops to its baseline value, which is indicative of another highly parallel state.

The magnitude of the resistance values and magnetic trends are expected when compared to literature, including the GMR ratio of 2.1% [2].

3.1.2 Wheatstone Bridge (WB) Electrical Measurements

CIP contact configurations also allow for a WB-type arrangement, whereby two current leads are separated by a single voltage lead on each side of the ring. While the behaviors of asymmetric bridges have been described previously in literature [3], this thesis exclusively investigates highly symmetric Wheatstone bridges.

The measured potential difference of the bridge can be described by the following equation:

$$V_{WB} = \left| \frac{R_4}{R_3 + R_4} - \frac{R_2^A + R_2^B}{R_1 + R_2^A + R_2^B} \right| \times (V_{2PT} + C) \tag{3.4}$$

For uniformity of comparison, the potential difference is divided by the source current to obtain a value with units of resistance:

$$R_{WB} = \frac{V_{WB}}{I_S} \tag{3.5}$$

Functionally, this nanoscale device involves two leads for a current input and two leads for a voltage output. Analytically, it may be more intuitive to think of the measurement as a voltage, since it is a differential measurement between the two halves of the ring and there is no actual current passing along the same path as the voltage.

A 4μm ring with 2:1 aspect ratio and 220nm linewidth (Figure 3-2) was measured (Figure 3-3b).

[F] At saturation, the resistance begins very low with resistances close to zero. This indicates that the electrical contacts are placed accurately in order to divide the ring into four equal quadrants, that the ring is in a state in which all four of the quadrants have similar resistance values, and the contact resistances of the electrodes are small.

[G] At approximately -100Oe, the resistance begins to increase slightly until remanence, indicating that there may be slight asymmetric relaxations of the magnetic moments due to shape defects in the absence of a strong magnetic

field.

[H] At 20Oe, the resistance quickly spikes to reach a maximum resistance value, or maximum imbalance in the two halves of the ring.

[I] At 50Oe, the resistance abruptly decreases back to a low value before increasing slowly.

[J] At 190Oe, the resistance abruptly decreases slightly.

[K] At 206Oe, the resistance abruptly increases by a small value before continuing to decrease on increasing the field.

Interestingly, changing the hard layer into an intermediate state and then changing the magnetization of the soft layer yields minor loops with various remanence resistance levels (Figure 3-3c). Considering a positive saturation, the lowest remanent state is obtained after applying a 23Oe field while the highest remanent state is obtained after applying a -40Oe field. A third remanent state is obtained after applying a -40Oe field followed by a 5Oe field.

A 2μm ring with 2:1 aspect ratio and 120nm linewidth was also measured (Figure 3-4).

[A] At saturation, the resistance is very low with two minor peaks until remanence. From positive saturation, the peaks occurred at 180Oe and 490Oe. From negative saturation, the peaks occurred at -460Oe and -230Oe.

[B] At -100Oe, the resistance begins to increase with field in a wavy step-like fashion until 20Oe when it abruptly decreases to a low value.

[C] At 150Oe, the resistance increases abruptly to the maximum resistance value.

[D] At 400Oe, the resistance decreases to an intermediate plateau.

[E] At 580Oe, the resistance drops near to the baseline value through several steps. From positive saturation, there is a step at -720Oe before the resistance

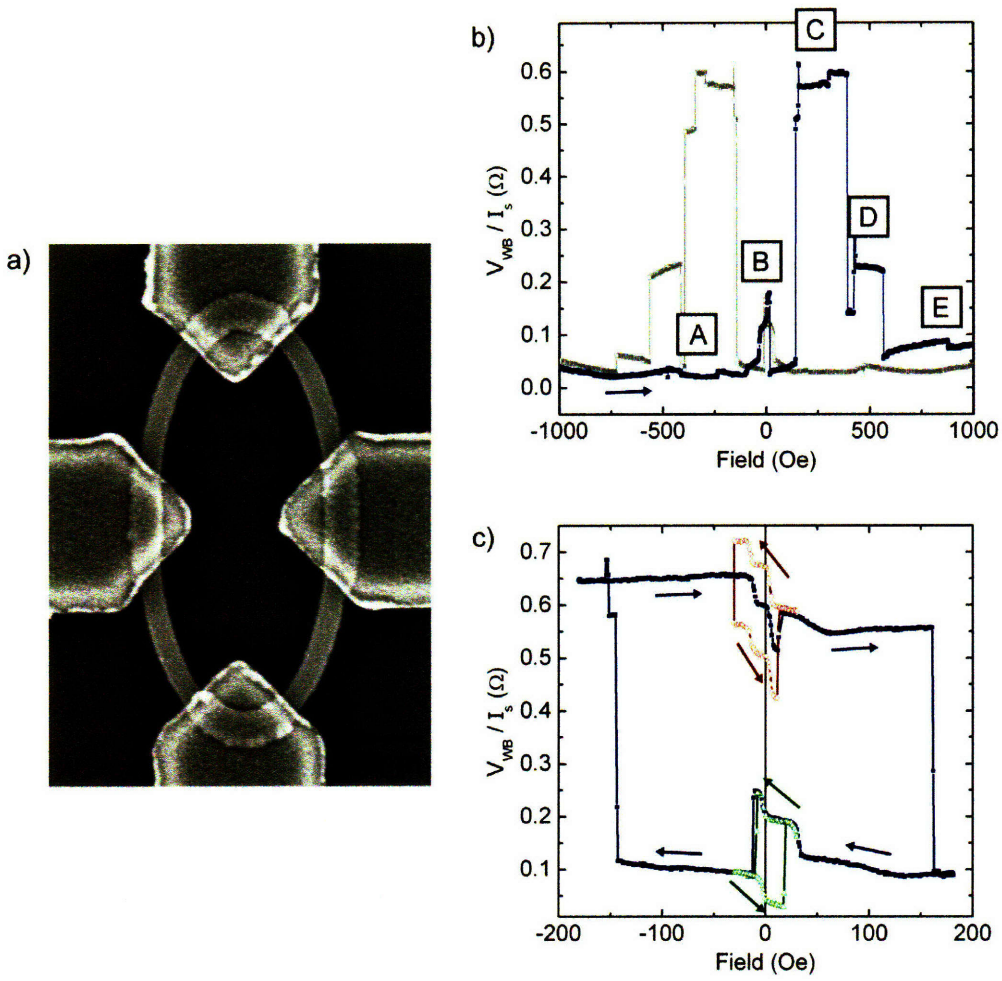

Figure 3-4: a) A scanning electron micrograph of a 2μm ring with a 2:1 aspect ratio and 120nm linewidth. b) The resistance versus field behavior of the ring from saturation and c) cycling at various lower fields after positive saturation.

decreases to the baseline value. From negative saturation, there is a step at 880Oe before the resistance decreases close to the baseline value.

Again, the WB arrangement yields several remanent resistance states when initiating a minor loop (Figure 3-4). Considering a positive saturation, the remanent states of the large loop are accessed by fields of 180Oe and -180Oe. Each large loop branch has two different remanent states that are accessed by fields of 30Oe and -30Oe.

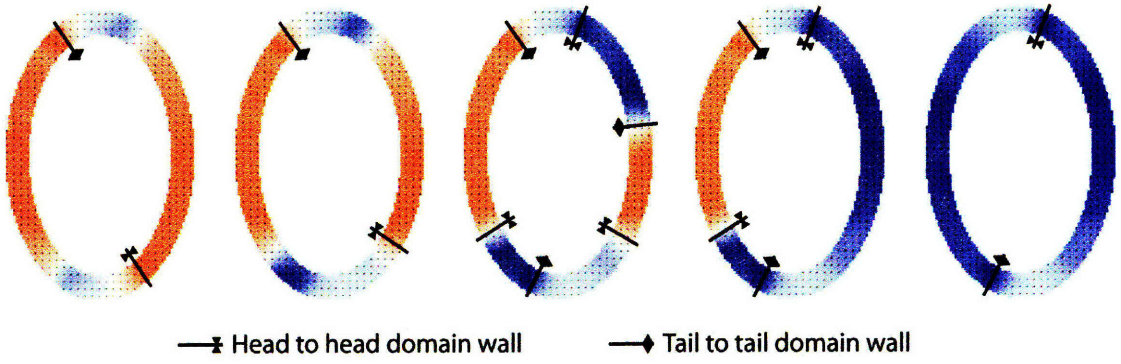

Figure 3-5: OOMMF snap shots of the soft layer reversal in a 600nm elliptical ring with a 3:2 aspect ratio and 50nm linewidth as a function of increasing field from left to right. These snapshots are representative of typical soft layer reversals, which begin with an off-center bi-domain state (left), that proceeds to reverse by nucleating two DWs at either end. The four DWs farthest from the ends of the ring propagate until the DWs meet, leaving only a reverse onion state (right).

3.2 Micromagnetic Modeling

The electrical behavior of multilayer rings is often believed to be the superposition of two single layer magnetic rings. In reality, there are much more intricate interactions between all of the different energies including magnetostatic coupling, exchange energy, shape anisotropy and external field. The experimental insights of symmetric WB contact configurations that amplify extremely small imbalances of magnetic behavior illustrate this complexity. Many rings were simulated, including those with outer diameters ranging from 150nm to 2μm, aspect ratios from 1:2 to 1:1, and widths ranging from 30nm to 200nm. Two general observations including the soft layer reversal mechanism and the stability of 360° DWs are described.

3.2.1 Soft Layer Reversal

After saturation, two of the DWs are present from the bi-domain onion state. As the saturation field is relaxed, these walls experience repulsion from the corresponding 180° DWs in the hard layer, and attain off-centered positions. Whether two walls move to the same half or to opposite half of the rings depends on the competition between the shape and the slight shift of the 180° DW in the hard layer. As a result it is difficult to predict for a given sample.

As the reverse field approaches zero, the magnetostatic coupling contributes to reversing the ring segments that have soft layer magnetizations perpendicular to the magnetization of the hard layer. As the field is further reversed, the field assists the rotation of the magnetizations until eventually new domains are nucleated and two DWs form at each end of the ring. These new domains are stabilized by the magnetostatic interactions with the hard layer, and are defined by the shape of the ring.

After this initial nucleation, the walls farthest from the ends propagate, effectively reversing the ring. This is very often an asymmetric propagation along the sides of the ring, with the extreme being that only one side propagates first, creating a pseudo-vortex state. There are often several quasi-stable configurations, which are assumed to exist from a combination of local shape defects, as well as by magnetostatic coupling. Once both sides of the rings reverse, the soft layer attains the final reverse onion state.

Stability of 360° Domain Walls

The asymmetry of the propagation in the soft layer allows the trapping of 360° DWs when two 180° DWs of different chiralities approach each other. In this system, the two DW chiralities are DWs that point toward the center of the ring and those that point away from the center. The locations of 360° DWs are highly dependent on local magnetization fluctuations of the hard layer, and are therefore assumed to be stabilized in formation by magnetostatic coupling. After a 360° DW is formed, it is stable to much higher fields despite the hard layer state.

As the field is further reversed, the hard layer tended to transition into an intermediate state between the onion and the reverse onion state. This intermediate state was either a vortex state or a state with reverse domains. The latter case results from the magnetization rotating in the long branches that are along the field lines and reverse from these parts of the ring. These reverse domains were typically formed such that between two and four 360° DWs are formed. These 360° DWs typically showed magnetic stability to fields greater than 1000Oe.

Vortex states were predicted to form in only a few cases in either the soft or hard layer. However, all of the simulated vortex states show that there tends to be a stable 360° DW present. This is a result of the reversal mechanism that has one bi-domain wall move to join with the other bi-domain wall that has a different chirality. There was no trend found as to whether a clockwise or counter-clockwise vortex had a preference of forming, or whether a head-to-head DW tended to move over a tail-to-tail DW.

3.3 Discussion

3.3.1 4μm Ring, 2:1 Aspect Ratio, 220nm Linewidth

The experimental 4PT response of the major loops generated from the two saturation polarities resembles that previously reported in literature [34]. However, the soft layer intermediate state attains resistance levels which are not half of the difference between the maximum and minimum resistance levels as expected had there been a vortex state (Figure 3-3[B]). Further, the resistance levels are different depending on the saturation polarity. While there may be slight asymmetries from magnetic field or fabrication defects, the micromagnetic prediction of soft layer response with four propagating DWs corroborates with the largest WB signal that occurs over this field range. This is only possible with the severe unbalancing of the two halves of the bridge. Had a vortex state been present, one would expect the WB to show a very small signal.

It is interesting to note that prior to the soft layer switching, the WB shows a gradually increasing signal with field (Figure 3-3[G]). Since the 4PT shows a flat baseline signal over this range, the WB effectively measures the slight movements of DWs and small regions of magnetization rotation. If the reversal occurs by the formation of four propagating DWs, then this signal corresponds to the bi-domain walls in the soft layer moving off-center, either to the same half of the ring or on opposite sides with one moving much more than the other.

Once the soft layer transitions completely into a reverse onion state, the 4PT resistance reaches a constant high resistance level where the two layers are in an antiparallel state (Figure 3-3[C]). The WB signal drops to its baseline value before increasing slightly with increasing field (Figure 3-3[I]), indicating a slight unbalancing of the bridge. The unbalance is attributed to the slight magnetization changes in the hard layer. This can arise from small shifts in the DWs or the gradual rotation of magnetic moments under the reverse field.

As the reverse field is increased, the 4PT measurements show that the hard layer transitions into an intermediate state (Figure 3-3[D]). Since this value is half of the difference between the maximum and minimum resistance values, it is consistent with a vortex state. The low WB signal is also indicative of a vortex state (Figure 3-3[J]).

This magnetic reversal is corroborated by micromagnetic simulations. While a simulation of a 4μm ring was not practical to perform computationally, there were many simulations that produced similar electrical responses. For clarity, this ring is compared to that of a 2μm elliptical ring with a 2:1 aspect ratio, 120nm linewidth and 8nm of Co (Figure 3-6).

The simulated soft layer response showed the formation of the four propagating DWs as the reversal mechanism. The bi-domain walls were off-center on the same half at remanence, and showed the formation of two 360DWs. The simulation showed that these 360° DWs were stable in the soft layer until fields of 500Oe. When the soft layer is in a reverse onion state, the WB signal decreases with increasing fields owing to the contraction of the 360° DWs (Figure 3-6[D]). However, the experimental device showed a baseline value in that field range (Figure 3-6[I]), and thus indicates that 360° DWs were not formed.

When the hard layer transitions into an intermediate state, the simulation suggests that it does so through the propagation of one of the DWs to the opposite end. Since these DWs have opposite chiralities – one is pointed into the ring and one is pointed out of the ring – a vortex state is formed with a stable 360° DW. Experimentally, 4PT measurements cannot distinguish the presence of 360° DWs, but the WB signal shows evidence for their existence.

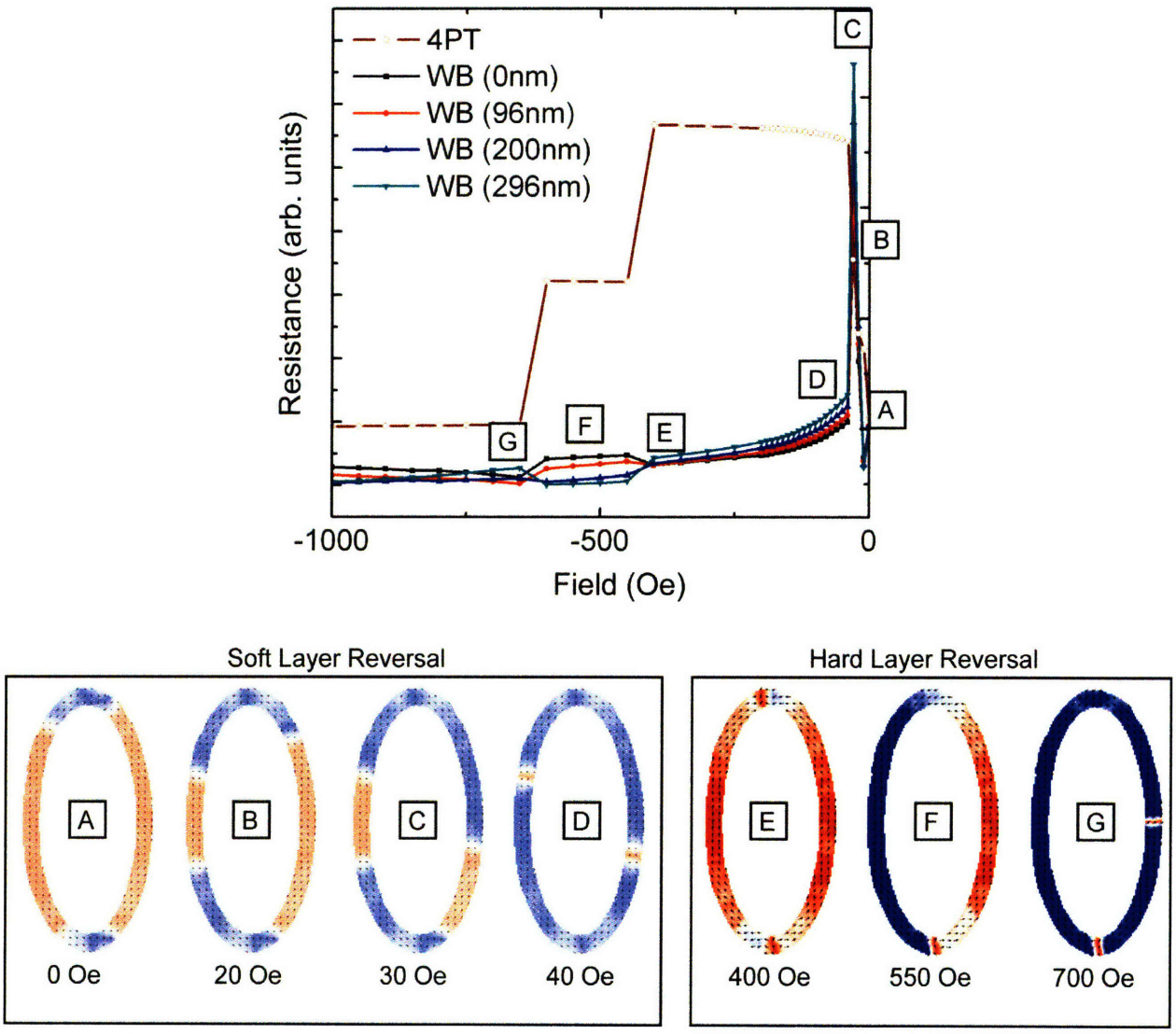

Figure 3-6: The simulated electrical response of a 2μm ring with 2:1 aspect ratio, 120nm linewidth and 8nm Co (top). The WB electrical response changes slightly as a function of contact width, identified in the graph legend by parentheses. The corresponding micromagnetic states at each predicted resistance level (bottom) in both the soft layer (left) and the hard layer (right).

When the hard layer transitions into the vortex state, the WB signal drops to a baseline value (Figure 3-6[J]). After the complete reversal of the hard layer into a reverse onion state, the WB resistance increases abruptly but slightly before decreasing with field (Figure 3-6[K]). Had there been no 360° DWs, the WB signal should remain constant at the baseline value from the vortex state until reverse saturation. The simulation suggests that a 360° DW was formed in the vortex state where an electrode would have been fabricated for electrode widths greater than 150nm. This results in a low, baseline WB signal. When the hard layer transitions into the reverse onion state, another 360° DW forms and a slightly higher WB signal is achieved. As the reverse field increases, the resistance decreases as the 360° DWs contract.

3.3.2 2μm Ring, 2:1 Aspect Ratio, 120nm Linewidth

The 2μm ring contacted in a WB arrangement acts much differently than the 4μm ring. No 4PT measurements were performed, but micromagnetic simulations predict the possible magnetic states that could produce the observed behavior. The ring was simulated as an idealized 2μm ring with a 2:1 aspect ratio, 120nm linewidth and 4nm Co. The trends in the soft and hard layers match the experimental results well (Figure 3-7).

The soft layer showed increased a step-like fashion in both experiment (Figure 3-4[B]) and in the simulation (Figure 3-7[A,B,C]). The simulation suggests that the ring follows the trend of soft layer reversals by nucleating and propagating four DWs. Each step in the resistance corresponds to a quasi-stable state where the propagating DWs become pinned. This progresses until the soft layer switches entirely to a reverse onion state, and the baseline resistance is reached again. Two 360° DWs are predicted to be trapped in the soft layer after the reversal.

The hard layer behavior showed a large increase to a stable resistance, and decreased in a step-like fashion in both experiment (Figure 3-4[C,D]) and in the simulation (Figure 3-7[E,F,G]). The simulation suggests that these steps exist because of a much different switching mechanism than a single DW propagating to form a vortex state. Rather, reversal occurs by the formation of four reverse domains which expand

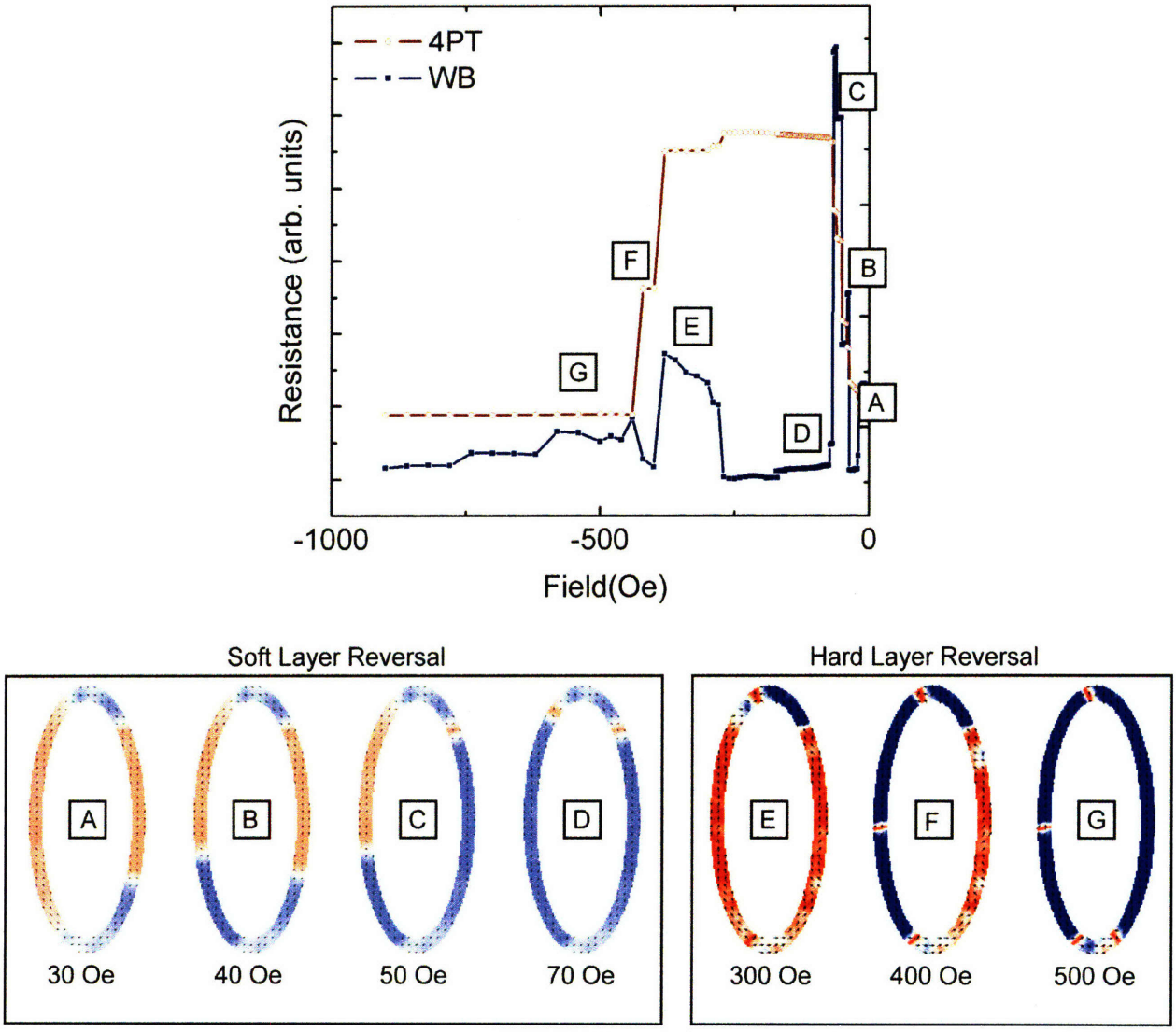

Figure 3-7: The simulated electrical response of a 2μm ring with 2:1 aspect ratio, 120nm linewidth and 4nm Co (top) and the corresponding micromagnetic states at each predicted resistance level (bottom).

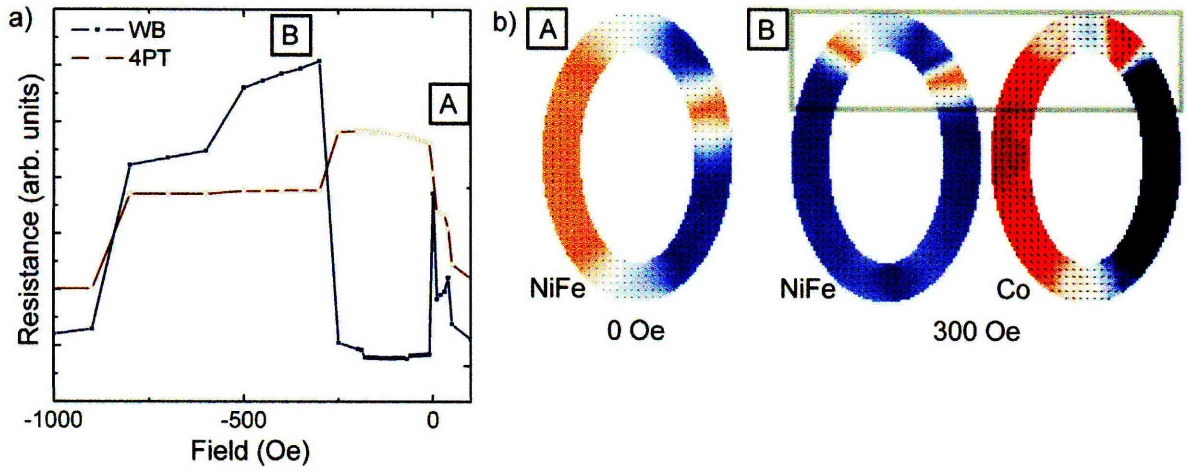

Figure 3-8: The simulated electrical response of a 600nm ring with 3:2 aspect ratio, 80nm linewidth and 4nm Co (left). The simulations reveal how a hard layer response can have a higher magnitude than the soft layer. In [A], the soft layer reverses through a vortex-like state which yields a small WB signal. In [B], the soft and hard layer 360° DWs are coupled and create large areas of high anti-alignment in a highly aligned vortex state.

and trap four 360° DWs. Domain creation and expansion does so in stages, which results in the observed steps.

The relative magnitudes of the peaks in the WB measurement cannot be explained by this particular simulation. However, comparing the ring to simulations of other sizes gives insight into how it may be possible to attain a larger WB signal from hard layer switching events than those from soft layer switching events. In a simulation of a 600nm long ring, 3:2 aspect ratio and 80nm width, there is a demonstration of a much larger hard layer signal (Figure 3-8). The soft layer reversal is much less pronounced since the four propagating DWs form more balanced states between the two halves, including a vortex-like state (Figure 3-8[A]).

Another factor is that there is a coupling between 360° DWs in the hard and soft layers (Figure 3-8[B]). In the soft layer reversal, the simulation shows the formation of a 360° DW near one of the ring ends. As the hard layer reverses, the soft layer 360° DW stabilizes a corresponding 360° DW adjacent to it in the hard layer. This effectively creates a large region of antiparallel alignment that amplifies the unbalance of the hard layer. As higher fields are applied, the 360° DWs contract at certain

critical fields in steps, which lead to the tiered decrease in resistance.

3.4 Wheatstone Bridge Based Devices

3.4.1 Data Storage

The use of magnetic elements in data storage requires distinct remanent resistance states that can be controllably changed either by an applied field or by spin-transfer torque. Regardless of the switching method, coercive fields should be small for practice device applications.

In both the 4μm and the 2μm rings contacted in the WB arrangement, there are at least two addressable remanent states that can serve as a '0' or '1'. The 4μm ring shows a minor loop that can be cycled to two remanent states with fields of -40Oe and 20Oe, which is sufficient for a single bit storage. While it has been demonstrated that three different remanent states are accessible (Figure 3-3c), ternary memory has not been shown to be particularly useful is thus not interesting to consider. On the other hand, the 2μm ring (Figure 3-4c) shows minor loops that can be cycled to between two and four different remanent states with very large signal changes. Thus, this element can be used as a 1-bit or 2-bit storage device.

3.4.2 Computer Logic

The concept of computer logic using currents as inputs, using a magnetoresistive element to perform a logic operation and generating a voltage output is fully compatible with the WB in elliptical rings. However, the rich WB response allows for two different kinds of logic that can be performed. The 2μm ring is used to illustrate the two types of logic since it has many more stable states to take advantage of (Figure 3-9).

The first method has been proposed in other magnetoelectronic devices and previously explained in Section 1.3.2. It consists of a gate programming step, a logic input step and a logic read step that are executed sequentially. In the The inputs are two fields A and B, with a field value of -15Oe corresponding to logical '0', and

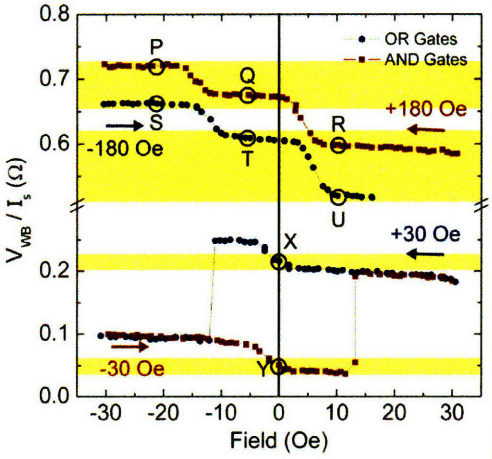

	Input				Output	
	Binary		Fields (Oe)		-180 Oe	+180 Oe
	A	B	A	B	A+B	OR	AND
Output "0"	0	0	-10	-10	-20	0 S	0 P
	0	1	-10	+5	-5	1 T	0 Q
	1	0	+5	-10	-5	1 T	0 Q
Output "1"	1	1	+5	+5	+10	1 U	1 R

	Input				Output	
	Binary		Fields (Oe)		+30 Oe	-30 Oe
	A	B	A	B	A+B	OR	AND
Output "0"	0	0	-15	-15	-30	0 Y	0 Y
	0	1	-15	+15	0	1 X	0 Y
	1	0	+15	-15	0	1 X	0 Y
Output "1"	1	1	+15	+15	+30	1 X	1 X

Figure 3-9: The low field response of the 2μm ring (left). The lower loop corresponds to the cycling of the soft layer with the hard layer in an onion state. The higher-resistance curves correspond to cycling of the soft layer with the hard layer in an intermediate state. Colored bands correspond to the assigned high and low resistance levels of the device. The logic table for the device with a separate logic write step, but simultaneous input and output steps (right top). The logic table for the device with separate logic write, logic input and logic output steps (right bottom).

+15Oe to logical '1'. The ring is initially positively saturated, then programmed at −30Oe (to give an 'AND' operation) or at +30Oe (to give 'OR'). Application of the two input fields then gives an output consisting of voltage level X ('0') or Y ('1'), which are measured at remanence after the input fields have been turned off. After each use, the gate function needs to be reset using another 30Oe programming step.

Instead of using a constant line of input through a clock cycle, the ability for the magnetoresistive unit to initiate the input and output at variable times in sequence could allow for more efficient computing since the logic unit only needs to be referenced when it is used. This has a great potential for energy-efficient computing since no power is required to maintain the magnetic device in a given logic, input or output state.

The second mode of operation does not require reprogramming after each operation and takes advantage of reversible, non-hysteretic movement of DWs along the length of the ring at low fields. The device is initially programmed using a field of −180Oe for 'OR', or +180Oe for 'AND'. The inputs A and B are fields of −10Oe ('0') or +5Oe ('1'). The output, which is the voltage measured while inputs A and B are being applied, can have one of six values (P, Q, R, S, T, and U) in which the lower voltage levels (R, T, U) correspond to logical '1' and the higher voltage levels (P, Q, S) to logical '0'.

This method of computer logic is more similar to current CMOS as the output is read at the same time as the input is supplied. The logic gate is still programmable prior to the logic operation, and retains that logic gate information until it is reprogrammed.

To estimate how effective these elements will be as devices, the power consumption and switching times can be estimated. For a nearby current-carrying write wire that is 200nm away from a ring element, the current is calculated to be 1mA − 5mA for low-field cycling (less than 50Oe) and 25mA − 35mA for high-field cycling (between 100Oe − 300Oe. These values are obtained by assuming that the wire is very long relative to the element size, and used an infinite wire approximation. Given a typical 1.8V supplied in integrated circuits, approximately 2mW−10mW of power is required

for low field-cycling while $40\text{mW} - 60\text{mW}$ is required for high-field switching. These power values are estimated to be up to two times higher for elements with 100nm in outer dimensions due to higher switching fields.

The actual power consumption for non-volatile schemes is much lower since magnetic elements only require power during read and write steps, and not to sustain the information. The switching time of an element can be approximated from the DW velocity, which is estimated to be around 50m/s in low-field cycling, and 150m/s in high-field cycling [5]. For the elements described in this thesis which have long dimensions of 2μm, switching times are on the order of 10ns for low-field cycling and 3ns for high-field switching. The application of write currents need to be supplied for at least as long as the switching time of an element. Thus, although the current doubles for high-field switching, the DW velocity triples resulting in lower overall power consumption per operation. Moreover, the switching time will decrease significantly for smaller elements, as DWs have less distance to travel to reverse an element completely.

3.4.3 Limitations and Considerations

Size

One of the most ubiquitous concerns in using elements for data storage or processing is how well the elements scale with size. Smaller elements are always sought to increase efficiency and density while reducing power consumption.

However, the magnetic behavior of elliptical rings changes as the size is scaled down. The first change is that the switching fields increase since the shape anisotropy dominates the energy. The second change is the change in magnetic switching mechanisms. The WB devices outlined in this chapter require a soft layer reversal mechanism that nucleates and propagates four DWs, and hard layer signals based on 360° DWs.

In the soft layer, the reversal mechanism is not found to persist in rings of sizes below 300nm in length for 3:2 aspect ratio elliptical rings according to scaling mi-

cromagnetic simulations performed (Figure 3-10). From the scaling information obtained, it appears as if the 6 domain wall (6DW) state containing 4 propagating DWs only appears if $0.10 <$ linewidth/long axis < 0.23. However, when the ring size is on the order of the simulated $120\text{nm} - 150\text{nm}$ DW width, it is impossible to reverse except through a vortex state.

There are also limitations in the ability to fabricate elements up to a certain size. Fundamentally, a ring can only scale down as small as can be physically fabricated. Since it is necessary to form a void in the center of an ellipse, the void defines the minimum feature size rather than the outer dimensions as in other geometries. In particular with CIP measurements, the ring size will be limited by the size of contacts that can be placed onto its surface. The difficulty of fabricating small and reproducible electrodes is a large motivating factor to use CPP devices, where the contacts above and below the ring can be arbitrarily large without affecting the magnetic signal. The smallest fabricated multi-layer rings with electrical contact are on the order of 150nm in their long axes [4], while the smallest fabricated single-layer ring elements have been made to 13nm.

Another consideration for contact sizes is electromigration and heating from the current densities required. Spin torque transfer schemes typically require $1 - 50\text{mA}$ of current in order to switch a magnetic element. External field schemes use current-carrying wires to generate a local field that typically supply $1 - 100\text{mA}$ of current. Both of these schemes will require larger currents as a ring decreases in size and increases in switching field.

Signal

The signal-to-noise ratios are higher in the WB contact configuration than in a traditional 4PT configuration. In the $4\mu\text{m}$ device, the ratio of the maximum signal to the magnitude of the noise is 77 for the WB configuration, while it is 30 for the 4PT configuration. This is since the contact resistances do not play as large of a role. In any given device, the electrical signals as a function of applied field are very reproducible (Figure 4-3).

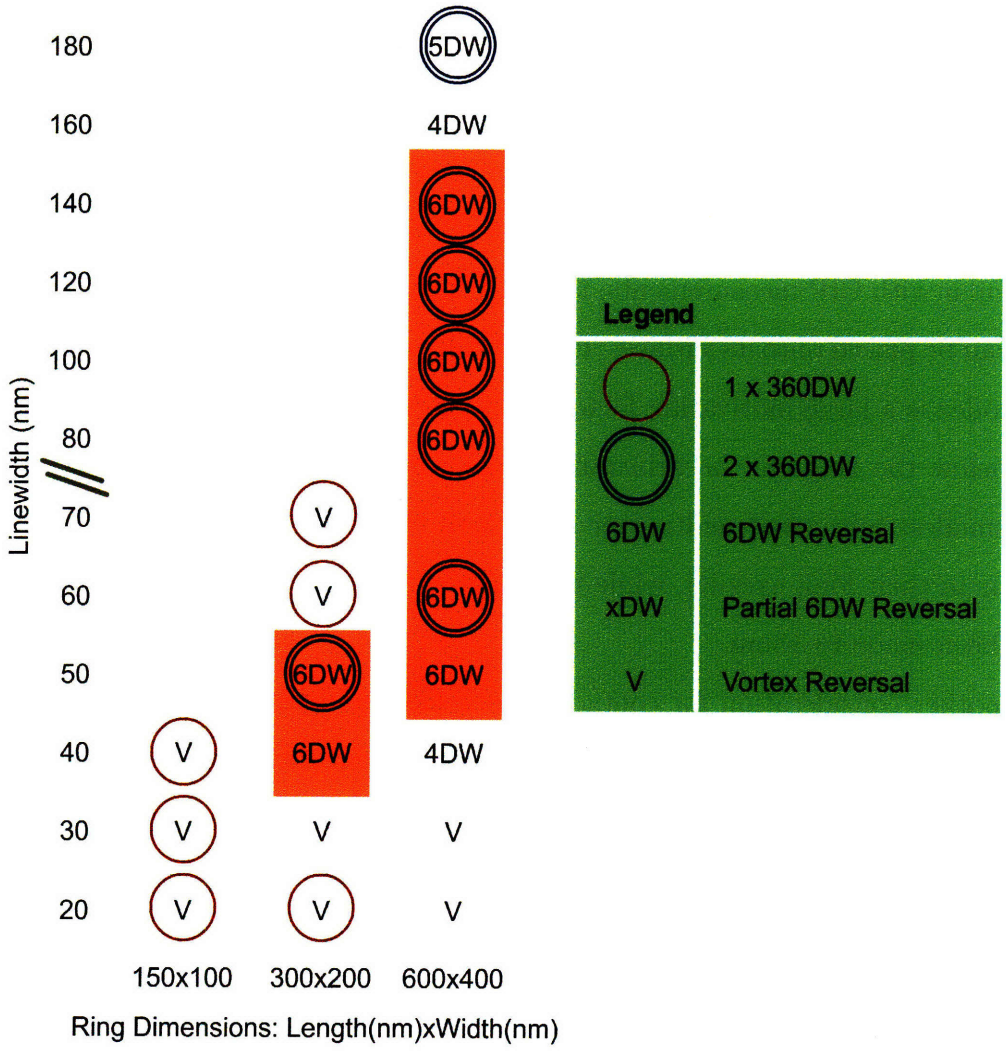

Figure 3-10: A summary of the scaling behavior in a variety of 3:2 aspect ratio elliptical rings with 8nm Co and a cell size of 5nmx5nmx4nm cell sizes. The red shading indicates the regions where the reversal mechanism involving the nucleation and propagation of four DWs proceeds normally.

However, WB devices are much more susceptible to fabrication defects since they utilize differential measurements. This plays a much larger role when the ring sizes are reduced, and contacts will probe smaller portions of the ring. It will presumably be more difficult to attain a relatively symmetric configuration. Thus, it is expected that random fabrication defects in the ellipses, contact size and contact position may cause variations in the signal magnitudes as well as the types of signals measured.

The actual signal produced by the WB devices is a voltage measurement that is on the order of mV, and are not expected to scale with larger currents since it is a differential measurement. Thus, there is no easy way to amplify the signal without also amplifying the noise. This is in contrast to probes of a pure magnetoresistance signal where current can be increased to provide a larger voltage signal. As a reference, CMOS processes currently use 5V as a high signal and 1V for a low signal.

3.5 Summary

Elliptical rings were experimentally measured with symmetric WBs, and compared with 4PT measurements. The WBs gave additional insight into the complexity of switching mechanisms in rings, and showed that certain mechanisms predicted through micromagnetic simulations are probable explanations of experiment. In particular, a large WB signal is induced by a typical soft layer reversal mechanism that involves the asymmetric nucleation and propagation of DWs from the two ends of the ring.

The rich WB signal was found to be highly reproducible within a sample. It was shown how these WB devices could be exploited in multi-bit memory, and used in power-efficient schemes to perform computer logic. The limitations and considerations of utilizing these in computing schemes were discussed.

References

[1] L.B. Valdes, "Resistivity measurements on Germanium for transistors," *Proceedings of the IRE*, vol. 42, no. 2, pp. 420-427, Feb. 1954.

[2] F.J. Castaño, C.A. Ross, C. Frandsen, A. Eilez, D. Gil, H.I. Smith, M. Redjdal and F.B. Humphrey, "Metastable states in magnetic nanorings," *Phys. Rev. B*, vol. 67, no. 18, pp. 184425, May 2003.

[3] D. Morecroft, F.J. Castaño, W. Jung, J. Feuchtwanger, C.A. Ross, "Influence of contact geometry on the magnetoresistance of ellipticalal rings," *Appl. Phys. Lett.*, vol. 88, no. 17, pp. 172508-3, Apr. 2006.

[4] Z.C. Wen, H.X. Wei and X.F. Han, "Patterned nanoring magnetic tunnel junctions," *Appl. Phys. Lett.*, vol. 91, no. 12, pp. 122511, Jan. 2008.

[5] G.S.D. Beach, C. Nistor, C. Knutson, M. Tsoi and J.L.Erskine, "Dynamics of field-driven domain-wall propagation in ferromagnetic nanowires," *Nat. Mat.*, vol. 4, pp. 741-744, Oct. 2005.

Chapter 4

Rhombic Magnetic Rings

Circular [1], elliptical [2], rectangular [3] and triangular [4] multi-layer annular geometries have been previously investigated with the primary intent of generating structures that have multiple stable and accessible magnetic states. One interesting and unexplored geometry is the rhombic ring, since it is very close in shape to the elliptical ring. Thus, DW nucleation and propagation should occur in a similar fashion except that the introduction of corners and straight edges will be better controlled. In this section, multi-layer rhombic rings with 1.6μm long axis, 1.0μm short axis and 120nm linewidths were fabricated, electrically measured, and compared with micromagnetic simulations.

4.1 Electrical Measurements

There were three different types of samples measured from saturation to yield major loops: NiFe(6)/Cu(4)/Co(5)/Au(4) sputtered (S5), NiFe(6)/Cu(4)/Co(5)/Au(4) evaporated (E5) and NiFe(6)/Cu(4)/Co(8)/Au(4) evaporated (E8) rhombic rings (Figure 4-1).

4PT measurements of S5 show that there are no stable intermediate states in either of the layers. Reversing from saturation, there is a single jump to a large resistance before returning to a baseline value – a behavior typical of elements that switch as a single domain. The evaporated elements have over 45Oe lower soft layer

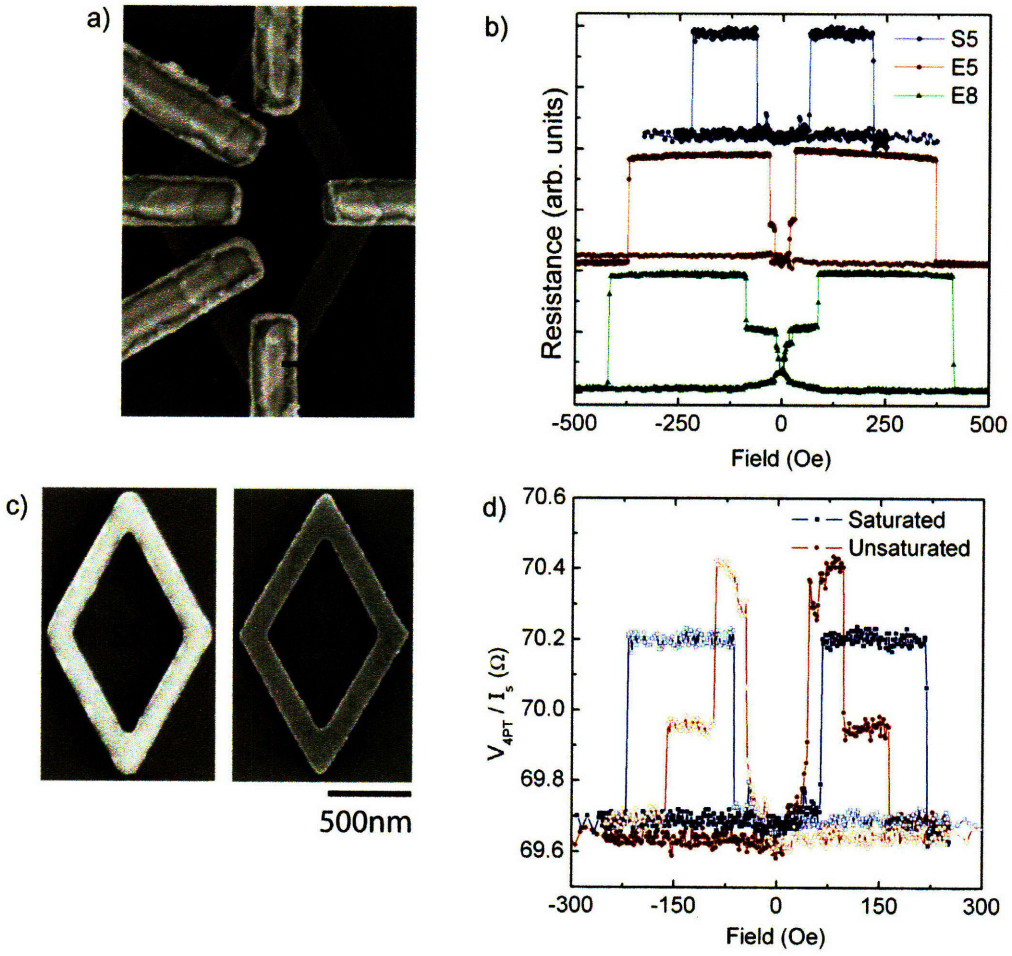

Figure 4-1: a) A scanning electron micrograph of a contacted rhombic ring device. b) 4PT electrical measurements comparing sputtered elements to evaporated elements. The results have been normalized and offset for ease of comparison. c) Scanning electron micrographs of a sputtered (S5) and an evaporated rhombic ring (E5). d) 4PT major loops of a sputtered element (S5) from a saturated state of approximately 5000Oe, and an unsaturated state of approximately 400Oe.

switching fields and at least 150Oe higher hard layer switching fields as compared to S5.

This indicates that the evaporated films exhibit stronger magnetostatic coupling between the layers, since any single layer tends to attain a state that is magnetically opposite to the other. There is also evidence of stable intermediate states in the soft layer, with E8 having a much more stable intermediate state than E5. This is expected since intermediate states are found to be more stable with strong magnetostatic coupling.

The GMR of 3.5% in E5 and 3.0% in E8 are much higher than the GMR of 0.9% in S5. The stronger coupling between the layers and the higher GMR ratios are indicative of better interfaces in the evaporated structures than in the sputtered structures. This can be attributed to a variety of factors, including subtle differences in the grain sizes, slight interdiffusion in sputtered samples due to high momentum atoms, slight crowning in sputtered samples, and small differences in the lifted-off geometries. The latter two fabrication differences are evident through the SEM images that show the sputtered element to have rounder corners and vertically protruding portions from crowned edges (Figure 4-1c).

Significantly different major loop behaviors are observed in S5 samples when they are saturated in a large field of approximately 5000Oe, as compared to an "unsaturated" state using a field of approximately 400Oe (Figure 4-1). Not only are the switching fields of both the soft and hard layer transitions much smaller in the unsaturated than the saturated loops, but there is evidence of a very stable intermediate state in the hard layer.

The fact that this not a true magnetoresistance measurement, but rather insight into the magnetoresistive state using a circuit analysis, becomes apparent when comparing the resistance magnitudes of the saturated and unsaturated loops. The unsaturated loops have both a lower baseline resistance and a higher maximum resistance. This is most likely not a result of a higher "magnetoresistance", but rather an indication that domain walls are trapped between the 4PT voltage probes in the unsaturated case, thereby scaling V_{2PT} by a different value in Equation 3.2.

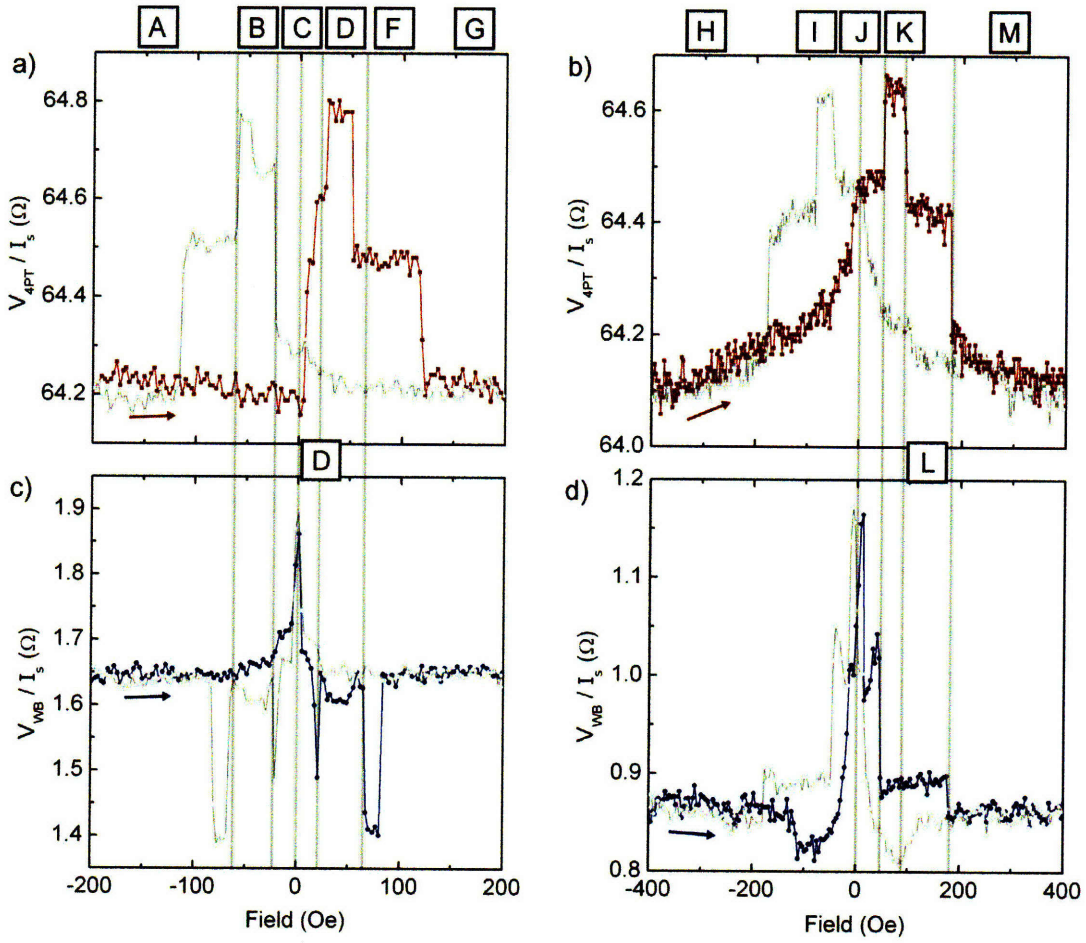

Figure 4-2: The easy axis (left) and hard axis (right) behaviors of S5 in both the WB (top) and 4PT (bottom) electrical configurations. All loops are generated from an unsaturated state with maximum field magnitudes of approximately 400Oe.

4PT and WB measurements were performed in three different S5 devices in both the easy and hard axes from the unsaturated state (Figure 4-2). The same overall switching behavior was observed in all devices, despite minor switching field differences of approximately 20Oe – 40Oe. Switching field variability is attributed to fabrication defects that change the pinning potentials of the walls.

It should be noted that the WB data, unlike in the elliptical rings, was not taken as the absolute value of the difference (Equation 3.4) but rather as a true differential resistance measurement. The baseline is produced from the contact resistance and is approximately 1.65Ω. Resistance values above the baseline represent a different polarity of voltage than resistance values below the baseline, and are referred to as

positive and negative potential differences respectively in this discussion.

4.1.1 Easy Axis

Two S5 devices were measured in the easy axis – one in the 4PT contact configuration and one in the WB contact configuration. The two devices produced electrical responses that correlated in terms of switching fields (Figure 4-2a,c):

[A] From a saturation field of 400Oe, both the 4PT and WB measurements produce constant baseline resistance states.

[B] At −60Oe, the WB resistance level increases gradually until remanence. From positive saturation, the 4PT resistance level also increases while from negative saturation, the resistance remains constant.

[C] At 0Oe, the WB produces a very large positive signal while the 4PT measurement increases rapidly.

[D] At 30Oe, the WB generates a very large negative signal, as the 4PT shows that the soft layer transitions through intermediate states.

[E] At 40Oe, the soft layer has completely switched, as evident in the maximum 4PT resistance, while the WB yields a small, constant negative signal.

[F] At 65Oe, the 4PT resistance level decreases to half of the difference between the maximum and minimum values, indicating that half of the ring is parallel. The WB generates the largest negative WB signal that is stable over a much larger field range as compared to the previous WB responses.

[G] At 110Oe, the resistance returns to the baseline values for both the 4PT and WB measurements.

The large WB signals, either positive or negative, occur at low fields but are only stable for such a small field range that the minor loop behavior was not investigated.

4.1.2 Hard Axis

Rhombic rings were measured electrically in the hard axis also in an unsaturated manner using 600Oe to produce symmetrical loops (Figure 4-2 right). This field is higher than that of the easy axis owing to the fact that larger fields are required to switch the hard layer.

The electrical behavior is found to be very similar to what one would expect for an elliptical ring:

[H] The resistance of the 4PT shows typical hard axis baseline with the resistance increasing as it approaches zero field and then decreasing at higher fields. The WB has a flat baseline.

[I] At −120Oe, the resistances in both the 4PT and WB show increases in resistance that increase more as the field approaches remanence.

[J] At 0Oe, the WB produces its largest signal for a small field range before decreasing to half of its original value. The 4PT transitions into a stable intermediate state.

[K] At 50Oe, the 4PT shows the largest resistance level while the WB drops to a small positive signal.

[L] At 90Oe, the 4PT resistance drops to half of the maximum and minimum values while the WB remains unchanged.

[M] At 190Oe, both the 4PT and WB fall back to their baseline signals.

Since the switching events in the hard axis WB occur over such a large range of field, it is possible to investigate the minor loop behavior of the element (Figure 4-3a). The device attains a highly reproducible minor loop with four distinguishable remanent states. The largest and smallest remanent resistances can be accessed by fields of 80Oe and −80Oe. Two intermediate remanent resistances are achievable using a sequence of fields that can be determined from the arrows in Figure 4-3a.

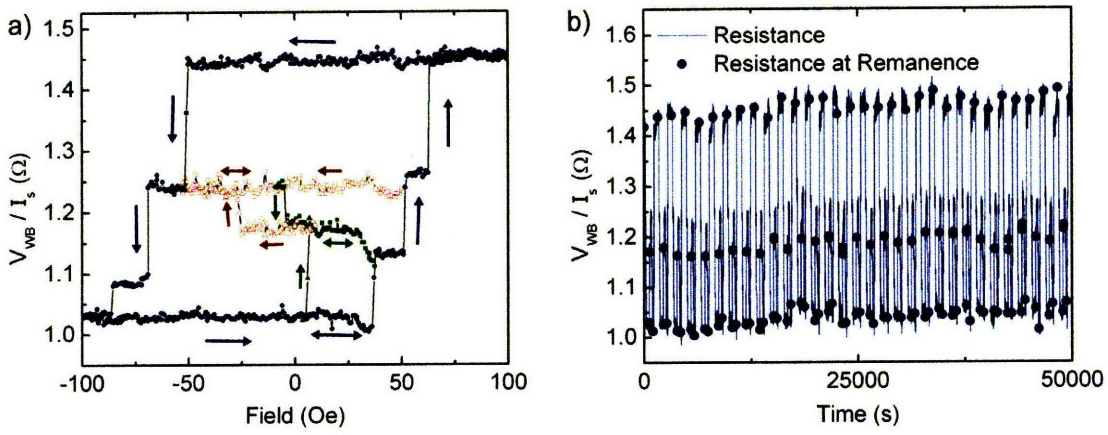

Figure 4-3: a) Minor loop cycling of S5 in a WB contact configuration after a negative saturation (left). Arrows indicate the field histories necessary to attain a particular trace. b) Low-frequency dynamics measurements of the minor loops were performed for over 50 loops over the span of days.

Examples are −80Oe, 20Oe to yield the lower intermediate resistance and −80Oe, 60Oe to yield the higher intermediate resistance.

Low frequency reproducibility measurements performing one cycle every 10mins are used to illustrate that three remanent states are easily accessible over many cycles (Figure 4-3b). All values tend to increase slightly over time, and is attributed to heating effects from the long measurements.

4.2 Micromagnetic Modeling

Micromagnetic models of these rings show that intermediate states do not correspond to a simple magnetic state, such as a vortex state, but rather are dominated by DW nucleation sites and areas that easily propagate DWs. There were general trends found in the soft and hard layer reversals. Ultimately, the reversal is found to be very similar to one that can occur in elliptical rings and is further classified in this section for rhombic rings.

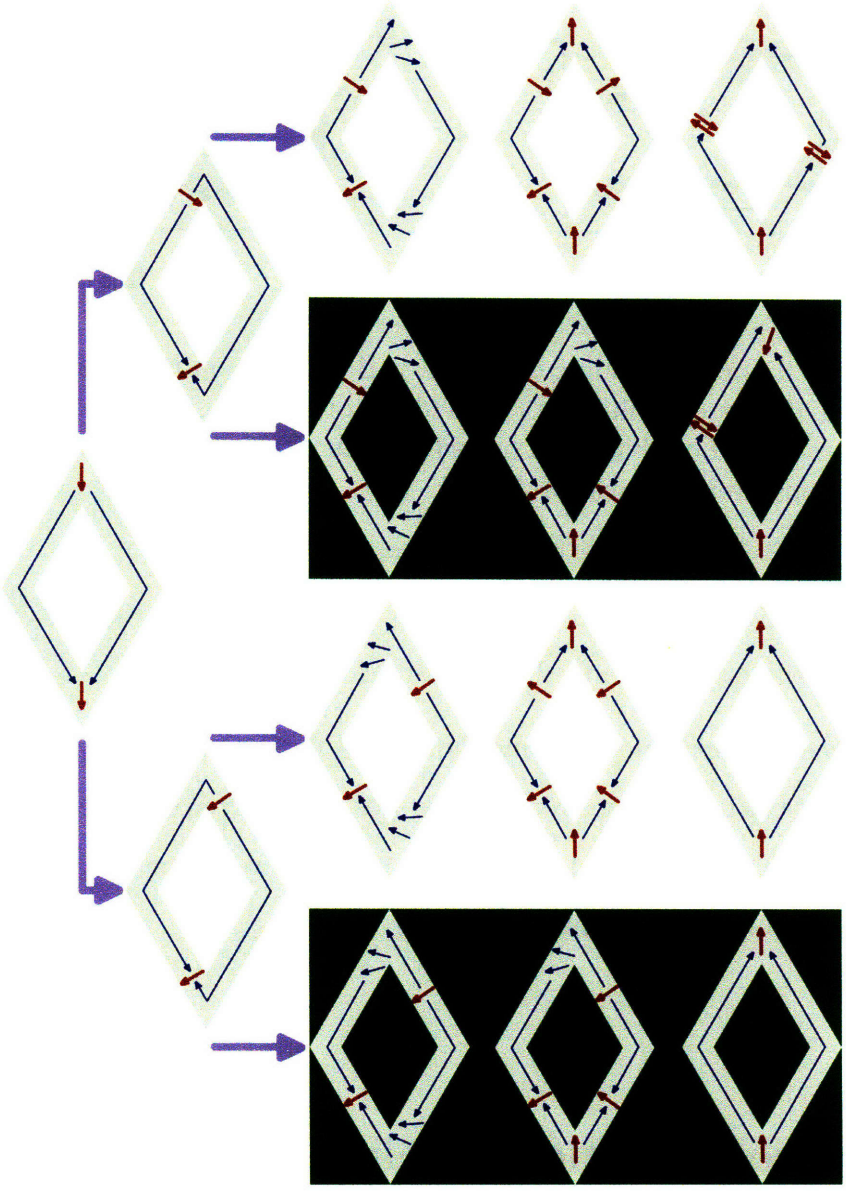

Figure 4-4: Soft layer reversal was found to proceed in very specific patterns. All states at saturation (left) proceed the reversal by shifting the walls off-center either to the same side or to different sides. As the field increases, DWs experience different pinning potentials, which vary whether both ends propagate, or only one side propagates to contribute to the reversal (right).

4.2.1 Soft Layer Reversal

Similar to the elliptical rings, the rhombic rings attain a bi-domain state after saturation (Figure 4-4). At low fields, the 180° DWs in the soft layer are repulsed from the corresponding 180° DWs in the hard layer, and reside outside of the vertex of the ring at the end of the rhomboid branches. Whether the two soft layer DWs occupy the same half of the ring is dependent on subtle details in the hard layer magnetic configurations, as well as shape defects. However, simulations suggest that the relative side that the domain wall resides on greatly changes the reversal mechanism.

As the reverse field is increased, the offset domain walls are free to propagate down the linear branches of the ring without a corner as a significant pinning potential. As in the elliptical ring, there is a pseudo-vortex-like state created around the vertex, where the magnetization lies along the ring. As the fields are increased, the magnetization begins to align with the applied field. At a critical field, the magnetic moments flip and create two DWs -- one at the vertex and one at the end of the rhomboid branch. The direction of the created DWs, either pointing toward or pointing away from the ring center, is determined by the position of the ring relative to the external field. It is opposite to the existing DW nucleated at saturation.

The walls furthest away from the vertices propagate asymmetrically until the propagating walls meet. The exact location in the ring where the walls meet is difficult to predict since it results from a combination of shape defects in the soft layer and magnetostatic interactions with the hard layer. In some cases, walls are nucleated and propagate much more easily on one side of the ring than the other, and thus only one end propagates its DWs to reverse the soft layer. 360° DWs result when two walls of different chiralities meet, such as when a DW pointing toward the ring center meets a DW pointing away from the ring center. Due to the reversal mechanisms, there are only 360° DWs when the two initial bi-domain walls begin off-center on the same side.

This reversal mechanism is very similar to the elliptical rings outlined in Section 3.3.2, which involves a bi-domain state that nucleates and propagates four DWs.

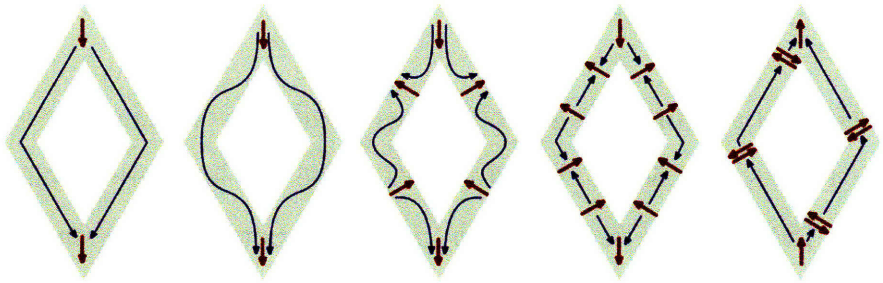

Figure 4-5: The hard layer reversal was found to proceed with one main mechanism throughout all simulations. The two-domains at the two ends bend the magnetization of any straight branch is perpendicular to the shape. At some field, additional DWs are nucleated, which propagate and join. The direction of the DWs, either pointed in or out of the ring, is predetermined by their position.

4.2.2 Hard Layer Reversal

The hard layer simulations show that reversal begins by the rotation of magnetizations in the straight segments of the ring to a magnetization that is perpendicular to the straight segment (Figure 4-5). This arises because of the strong alignment of the magnetizations at the vertices that lie along the easy axis and are highly stable from large shape anisotropy. Magnetization along the straight segments effectively rotates with the field with the magnetizations in the vertices fixed, thereby producing a systematic wavy pattern. It is found that the two straight branches close to the head-to-head DW nucleate DWs that point toward the center of the ring, whereas the two straight branches close to the tail-to-tail DW nucleate DWs that point away from the center of the ring.

As the field is reversed, different pinning potentials allow certain DWs to propagate and combine. Since DWs with different chiralities combine to form 360° DWs, it is typical to see four 360° DWs in the hard layer.

The specific behavior reversal at the vertices has shown various behaviors. Each vertex already has a DW present. If it attains an off-center position, then it tends to collapse into a 360° DW when it meets with a propagating 180° DW of a different chirality. The propagating DW on the other side moves to fill the reverse bi-domain position. However, in a completely symmetric ring where the DW is centered on the vertex, there is evidence that it should be possible to stabilize a 540° DWs when two

propagating 180° DWs converge at the vertex.

4.3 Discussion

4.3.1 Easy Axis

The rhombic ring was simulated using an SEM of a device, including dimensions of 2μm long axis 1μm short axis and 120nm linewidth. The soft layer reversed by having the DWs from the onion state move to off-centered positions on opposite sides (Figure 4-6). The tail-to-tail DW was pinned by the local magnetization of the hard layer, and so reversal occurred by the DW propagation from only one side of the ring as in lowest panel of Figure 4-4. As a result, there are no 360° DWs predicted to be trapped in the soft layer.

The propagation of the two moving DWs proceeds asymmetrically. Initially from saturation, the slight movements of the onion state DWs cause an initial large signal. As two other DWs are nucleated, the two propagating DWs do so asymmetrically. As one wall propagates, the signal is decreased slightly. As the other DW begins to propagate, the bridge is again unbalanced. However, since the reversal is on the other half of the ring, there is a large signal with the opposite polarity before the WB reading returns to a baseline value.

The hard layer switches by the rotation of moments in the linear branches, which causes domains to form in the middle of each branch. There is initially no observable signal due to the magnetostatic coupling that aligns the soft layer to the rotated hard layer. There is a large WB signal when the majority of the domains have reversed except for regions by the vertices that serve as asymmetric pinning sites for DWs. At a sufficiently high field, the 180° DWs join into four 360° DWs while the majority of the ring has attained a reverse onion state. As the field is further increased, the 360° DWs contract bringing the two 180° components closer together.

The simulated electrical response is calculated without taking an absolute value as in Equation 3.4. However, in doing so, there is an arbitrary assignment of whether

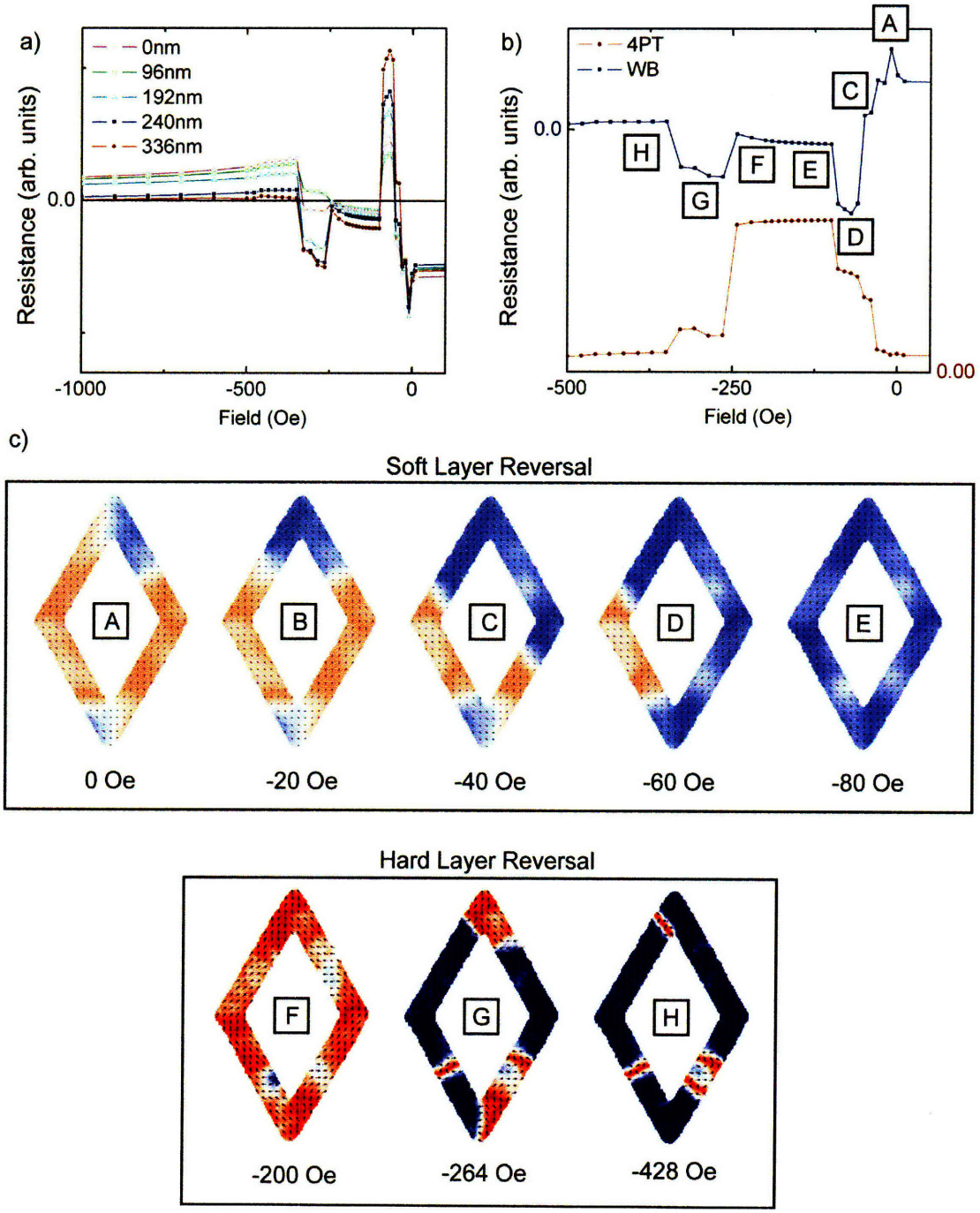

Figure 4-6: The simulated electrical response of a 2μm rhombic ring with 120nm linewidth. a) The WB response as a function of contact width, and b) the WB response taking a different reference in the soft layer than the hard layer as compared to the 4PT response. c) OOMMF snapshots of both the soft and hard layers show the magnetic states that correspond to each part of the simulated electrical response.

a signal will be a positive or negative value. Since the soft and hard layer reverse at significantly different fields, the positive and negative trends in each layer can be assumed to be independent of the other layer (Figure 4-6 Top). Reversing the polarity of the soft layer produces an electrical signal that is very similar to that obtained experimentally.

4.4 Conclusions

Major loops indicate that intermediate states in both the soft layer and hard layer are less stable from saturation. However, cycling the rhombic rings from an unsaturated state yields very different switching behaviors including significantly lower switching fields in both the soft and hard layers, as well as a very stable intermediate state in the hard layer.

Simulations suggest that the rhombic ring has magnetic configurations that are much more predictable as compared to the elliptical ring since DWs pin more readily at corners. As such, the reversal mechanisms in both the soft and hard layers are conducive to the formation of 360° DWs that remain stable until fields of over 1000Oe. These walls are most likely responsible for the different magnetic behaviors from different saturation fields.

References

[1] C.A. Ross, F.J. Castaño, D. Morecroft, W. Jung, H.I. Smith, T.A. Moore, T.J. Hayward, J.A.C. Bland, T.J. Bromwich and A.K. Petford-Long, "Mesoscopic thin-film magnetic rings," *J. Appl. Phys.*, vol. 99, no. 8, pp. 08S501, Apr. 2006.

[2] F.J. Castaño, C.A. Ross, C. Frandsen, A. Eilez, D. Gil, H.I. Smith, M. Redjdal and F.B. Humphrey, "Metastable states in magnetic nanorings," *Phys. Rev. B*, vol. 67, no. 18, pp. 184425, May 2003.

[3] C.C. Wang, S. Jain and A.O. Adeyeye, "Magnetoresistance dependence on electrical contact geometry and field alignment in mesoscopic rectangular rings," *Euro. Phys. J. B*, vol. 62, no. 3, pp. 305-309, Apr. 2008.

[4] A. Westphalen, A. Schumann, A. Remhof, H. Zabel, T. Last and U. Kunze, "Magnetization reversal of equilateral Fe triangles," *Phys. Rev. B*, vol. 74, no. 10, pp. 104417, Sep. 2006.

Chapter 5

Conclusions and Future Work

5.1 Conclusions

WB electrical measurements provided new insight into the magnetic reversal mechanisms of multi-layer rings. Micromagnetic simulations were able to explain the electrical signals with probable magnetization configurations at each field step. For the elliptic PSV rings under investigation, it was found that the magnetization reversal is not as simple as is often described in literature.

In the soft layer, a reversal mechanism was identified that involved the nucleation and propagation of four DWs. In the hard layer, four reverse domains form and collapse into four 360° DWs at high fields. These two reversal events yield large WB signals and multiple remanent WB resistance levels at very low fields. Thus, these devices were evaluated as storage and logic devices. The main practical limitations are reproducibility among different devices, and the small output voltages despite the large signal-to-noise ratios.

While these particular reversal mechanisms were simulated to exist in a variety of elliptical rings, the DWs were not positionally controllable. Rhombic rings have not been previously investigated, and were found to reverse with a similar mechanism as elliptic rings. However, the introduced corners and edges controlled the nucleation, propagation and positioning of DWs much more predictably. In particular, 360° DWs were found to have a much larger impact on switching than in elliptical rings.

Magnetic cycling from unsaturated states reversed at much lower fields by decoupling each 360° DW wall into a reverse domain, thereby circumventing DW nucleation. As a result, rhombic rings are useful as magnetoresistive devices that can perform functions at very low fields.

5.2 Future Work

5.2.1 Field-Induced Magnetic Reversal

There is still much to know about field-induced magnetic reversals in PSV ring devices. This thesis outlined the study of different dimensions that may play a role in determining whether one reversal mechanism is favored over another, namely (linewidth):(outer dimension length) for a given aspect ratio. However, there are other factors that influence the reversal such as magnetostatic coupling, and the ratio of the domain wall size to the element size.

After desirable magnetic states and reversal mechanisms are chosen, it should be possible to engineer the geometry of a device. Simulations and mathematical modeling can aid in this guided search. Another technique is to introduce asymmetries into the device that will favor certain states.

Regardless of studies performed, there are several improvements that are suggested for the magnetoresistance measurement setup to aid in device characterization:

- The concurrent data collection of both 4PT and WB data for any major or minor loop. This is especially important for studying 4PT minor loops since the WB gives additional insight to DW positions. The WB should be taken as a true differential measurement without taking the absolute value in order to gain insights as to which side of the ring reverses first. It might be interesting to see if this is a stochastic process.

- The ability to cycle fields at much higher frequencies to allow for the statistical analysis of switching behaviors. This is important when considering 360° DWs, since these walls greatly change the reversal from an unsaturated state.

- Automated angular rotation can test different axes more easily. This will be useful to determine the switching mechanism tolerance the relative angle between the easy axis and the applied field. It is expected that different angles produce different dominant reversal mechanisms. Angular studies can also be performed such as setting the hard layer into a state equilibrated at a different angle as soft layer cycling. For example, if the hard layer is saturated and maintained in the easy axis and then a smaller field at a small angle from the easy axis, then the soft layer reversal might be more controlled.

5.2.2 Understanding and Controlling 360° Domain Walls

360° DWs are found to be unusually stable in both multi-layer elliptic and rhombic ring structures. They are simulated to persist until over fields of 1000Oe in the hard layer. These types of walls are useful in devices since they circumvent the need to nucleate domain walls upon reversal. This has large implications in device applications if they can be precisely positioned, and act the same way over many field cycles. However, it is unclear as to why these walls choose to stabilize in certain sections of a ring, and why some 360° DWs are stable up to higher fields than others.

Insights from mathematical modeling may help to explain why these walls are stabilized, offer insights on how to position them accurately and ultimately how to control them. It will be insightful to verify those insights experimentally, such as through in situ magnetic force microscopy studies.

5.2.3 Current-Induced Magnetic Reversal

Only field-induced magnetic reversals were considered in this thesis. However, there is increasing interest in magnetic devices that are reversed using spin-torque transfer due to the small power consumption and the elimination of area effects from applying fields with current-carrying wires. However, field and current reverse rings differently – field causes domains in the direction of the applied field to grow, whereas current moves domains in the direction of electron motion.

In rings, spin-torque transfer has been found to work well in propagating one DW in a bi-domain state to form vortex states. Certain chiralities of vortex states can be controlled using CPP devices, since current passing through an element also exert an Oersted field. However, there have not been any studies using the reversal mechanism outlined in this thesis, which involves the presence of many more domain walls.

Preliminary studies should address whether 360° DWs can be moved by current, or whether the current will tend to collapse the DW. This may be probed by WB measurements, focusing observations under large applied field where 360° DWs are measured, such as in Figure 3-4[D,E]. Alternatively, DWs can be imaged at remanence through such techniques as magnetic force microscopy and scanning electron microscopy with polarization analysis.

If 360° DWs can be moved by current, then spin-torque transfer may provide a convenient way of controlling the magnetic reversal in a ring, even among differently fabricated devices. Since 360° DWs do not form in well-known positions, they can be induced to form and then be moved to one end of the ring by current. These current pulses may require an appropriate bias field in order to promote switching [1]. The reversal will begin from one end that is saturated with 360° DWs. Multiple 360° DWs collected at the end would collapse into one reverse domain at remanence. As a result, reversals would be much better controlled while still benefiting from low reverse fields since DWs do not need to be nucleated. Thus, a combination of field and current studies in sequence may yield potential for controlling device behavior.

5.2.4 Magnetostatically Coupled Devices

Magnetostatic coupling between the soft and hard layers has a significant influence on the reversal mechanism. It is a large factor on the existence of the four propagating DW reversal mechanism, and is conjectured to be the reason for highly stable 360° DWs. However, adding in the magnetostatic interactions with adjacent elements or biasing elements may yield interesting behaviors.

DW movement in the soft layer reversal that forms four propagating DWs from saturation is heavily dependent on the initial bi-domain wall positions, including

whether the DWs shift off-center to the same side or to different sides. If the magnetic interactions with adjacent elements can predictably influence the positioning of the DWs, then there may be more interesting and controlled magnetic reversals. This has implications for device applications if the biasing element can be changed or turned on and off.

5.2.5 Frequency

Most of the work that has been done in multi-layer rings has been in magnetostatic measurements. There are still many things to explore with dynamics, including studying the resonance of both 180° and 360° DWs, as well as investigating the properties of spin waves.

References

[1] D. Morecroft, I.A. Colin, F. J. Castaño, J.A.C. Bland and C. A. Ross, "Current-induced magnetization reversal in NiFe/Cu/Co/Au notched mesoscopic bars," *Phys. Rev. B*, vol. 76, no. 5, pp. 054449, Aug. 2007.

Appendix A

OOMMF .mif File

```
# OOMMF MIF 2.1
# Ross Group configuration file for PSV elements
# Last modified by Bryan Ng on 05/18/08

# User Inputs
# XRNG: The measured width, or x length in meters
# YRNG: The measured height, or y length in meters
# SampleID: The name of the simulation

# Constants
set PI [expr {4*atan(1.)}]
set MU0 [expr {4*$PI*1e-7}]

# Create individual layers
# x,y,z = width,height,depth according to your input file
# z represents where in 3D your layer starts and ends
Specify Oxs_ImageAtlas:layer1 {
   xrange {0 XRNG}
   yrange {0 YRNG}
   zrange {0 4e-9}
   image SampleID.bmp
   viewplane "xy"
   colormap {
      white nonmagnetic
      black Co
   }
}
```

```
Specify Oxs_ImageAtlas:layer2 {
   xrange {0 XRNG}
   yrange {0 YRNG}
   zrange {4e-9 8e-9}
   image SampleID.bmp
   viewplane "xy"
   colormap {
      white nonmagnetic
      black Cu
   }
}

Specify Oxs_ImageAtlas:layer3 {
   xrange {0 XRNG}
   yrange {0 YRNG}
   zrange {8e-9 12e-9}
   image SampleID.bmp
   viewplane "xy"
   colormap {
      white nonmagnetic
      black NiFe
   }
}


# Create a multilayer stack of the layers you just defined
Specify Oxs_MultiAtlas:stack {
   atlas :layer1
   atlas :layer2
   atlas :layer3
}

# Simulation mesh size
# Should be on the order of the exchange length of the materials (4nm for PSV)
# Except for elements where the mesh size is on the order of the element size
Specify Oxs_RectangularMesh:mesh {
   cellsize {4e-9 4e-9 4e-9}
   atlas :stack
}

# Exchange energy terms:
Specify Oxs_Exchange6Ngbr:NiFe {
   atlas :stack
   default_A 13e-12
   A {
```

```
      NiFe nonmagnetic 0
      NiFe Cu 0
      Co nonmagnetic 0
      Co Cu 0
      Co Co 30e-12
   }
}

# Anisotropy energy terms:
Specify Oxs_UniaxialAnisotropy {
   K1 {
      Oxs_AtlasScalarField {
         atlas :stack
         values {
            nonmagnetic 0
            Co 520e3
     NiFe 500
     Cu 0
         }
      }
   }
# Random in-plane vector field to simulate a polycrystalline film
   axis {
      Oxs_PlaneRandomVectorField {
         min_norm 1.0
         max_norm 1.0
         plane_normal {0 0 1}
      }
   }
}

Specify Oxs_Demag {}

# Set the magnetic field sequence
# {x1 y1 z1 x2 y2 z2 steps}
Specify Oxs_UZeeman [subst {
   multiplier [expr {1/$MU0}]
   Hrange {
      {5 0 0 0.001 0 0 1}
      {0.000 0 0 -0.020 0 0 20}
   }
}]

# Standard LLG constants
Specify Oxs_EulerEvolve:evolve {
```

```
   do_precess 1
   gamma_LL 2.21e5
   alpha 0.5
}

# Simluation details
Specify Oxs_TimeDriver {
   basename SampleID
   vector_field_output_format {binary 4}
   scalar_output_format %.15g
   evolver :evolve
   mesh :mesh
   stopping_dm_dt 0.12174983010168183
   stage_count_check 51
   Ms {
      Oxs_AtlasScalarField {
         atlas :stack
         values {
            nonmagnetic 0
            Cu 0
            NiFe 860E3
            Co 1400E3
         }
      }
   }
   m0 {
      Oxs_RandomVectorField { min_norm 1  max_norm 1 }
   }
}

Ignore {
  totalfieldoutputformat: binary 4
}

# Automatically archive the equilibrium state
Destination archive mmArchive
Schedule Oxs_TimeDriver::Magnetization archive stage 1
Schedule DataTable archive stage 1
```